Final Report Template

Project Title:	Rapid Development of Hybrid Perovskites and Novel Tandem Architectures
Project Period:	9/30/14 – 10/31/18
Project Budget:	$1,666,667
Submission Date:	12/15/18
Recipient:	University of Washington
Address:	4333 Brooklyn Ave NE, 17th Floor Seattle, WA 98195-9472
Award Number:	DE-EE0006710
Project Team:	Hugh W. Hillhouse and Alex K-Y-. Jen
Contacts:	Hugh W. Hillhouse Rehnberg Professor Phone: (206) 685-5257 Email: h2@uw.edu

Acknowledgment: "This material is based upon work supported by the Department of Energy under award number DE-EE0006710"

Executive Summary:

Multijunction solar cells based on epitaxially grown III-V materials hold the record for solar energy power conversion efficiency (PCE). However, due to the high cost of fabricating these devices, they are typically only used for concentrator cells and space applications. The overarching goal of this project was to develop low-cost printable hybrid perovskite (HP) materials appropriate and optimized for tandem solar cells with high power conversion efficiency under "1 Sun" illumination. Key results and findings over the course of the project we:

- Developed higher-performance high-bandgap (1.75 eV) perovskite materials and devices. In particular, we explored tens-of-thousands of compositions for high bandgap perovskites, achieving quasi-Fermi level splitting of 1.35 eV for a 1.75 eV bandgap material. We achieved World-record open circuit voltages from single junction p-i-n devices, 1.24 V from 1.75 eV bandgap material, which is what is preferable for tandems with a PCE of 14.3% using a guanidinium/formanadinium/ cesium alloyed lead iodobromide. We also developed a series of World-record efficiency devices at higher band-gaps based on 2D/3D perovskites using PEA.
- Developed higher-performance low-bandgap (1.35 eV) perovskite materials and devices. In particular, we developed a 1.35 eV bandgap perovskite of composition $MAPb_{0.5}Sn_{0.5}(I_{0.8}Br_{0.2})_3$ and showed its superiority to $MAPb_{0.75}Sn_{0.25}I_3$. High efficiency solar cells were fabricated using PEDOT:PSS and doped-ICBA as HTL and ETL, respectively. Short circuit currents of 25.7 mA/cm^2 and PCEs of 17.1% were obtained.
- Developed mechanically stacked 4-terminal CIGS-Perovskite tandems with PCE of 18.8% and monolithic 2-terminal CIGS-Perovskite tandems with PCE of 8.5%. The low efficiency of the monolithic device is a result of the high surface roughness of the solution processed CIGS bottom cells. This is not an intrinsic problem for CIGS-perovskite tandems, but does mean that smooth evaporated or sputtered CIGS films likely need to be used, unless a polishing step is employed.
- Developed monolithic 2-terminal Perovskite-Perovskite tandems with a stabilized PCE of 18.5%. This was the World-record perovskite-perovskite monolithic tandems for over a year in 2017-2018.
- Revealed that light is not an essential component of the so-called "light-induced" phase segregation. By using charge injection in the dark and electroluminescence, we showed that the presence of electrons in the conduction band and hole in the valence band is sufficient to drive the nearly ubiquitously observed phase segregation in high bandgap perovskites.
- Developed a new method to simultaneously measure absolute intensity photoluminescence and photoconductivity and use them to obtain simultaneous in-situ measurement of quasi-Fermi level splitting and diffusion length. This is important since it provides a proxy for device Voc and device Jsc.

In addition, 67 papers were published with support from this award that detail many more advances in the field, including numerous publications in high impact journals such as *Nature Photonics*, *Advanced Materials, ACS Energy Letters,* and *Energy and Environmental Science*.

Table of Contents

Background 3

Introduction 7

Project Results and Discussion 8

Conclusions 30

Budget and Schedule 31

Path Forward 32

Publications Resulting from this Work 33

References 37

Background:

The hybrid perovskites (HPs) are a recently discovered material class with potential to meet the global electricity demand at low cost. Power conversion efficiencies (PCEs) of HP solar cells have increased faster than any other PV material in history, and HP devices do not require use of any rare or expensive elements.[1-3] Cells can be fabricated from low temperature (< 150 ˚C) solution processing, indicating that CAPEX up to an order of magnitude lower than c-Si is possible[4]. Open-circuit voltages (V_{OC}) from completed devices of the 1.6 eV HPs have reached 92% of their detailed-balance maximum ($V_{OC,SQ}$).[3] The limited effect of non-radiative recombination in HPs despite fabrication via solution processing have shown that energetically favored intrinsic defects do not create effective Shockley-Read-Hall recombination centers[5-7]. Either their populations are low, they have small capture cross-sections due to the large dielectric constant of HPs, or their energy levels lie close to the band edges or within the bands themselves. This “defect tolerance” in HPs has been attributed to the orbital character of the band extrema (CB minimum consisting of bonding orbitals with the VB maximum consisting of antibonding orbitals – opposite of typical semiconductors), the low charge carrier effective masses, and the high static dielectric constant[8-11]

An intriguing and exceptionally useful quality the HP material class is its compositional variation leading to tunability of material properties. HPs have stoichiometry ABX_3, where A may be an organic or inorganic monovalent cation such as methylammonium (MA^+), formamidinium (FA^+), or cesium (Cs^+), the B site is a divalent metal cation (usually Pb^{+2} or Sn^{+2}), and X is a monovalent anion, typically I or Br. Since each lattice site can be continuously alloyed between different ions, the HP material class has an endless composition space contributing to the material versatility. For example, as the X site is alloyed from pure I^- to pure Br^- in $MAPbX_3$, the material bandgap (E_g) changes continuously from 1.6eV to 2.3eV[12]. Further, for $(FA,Cs)BI_3$, as B is changed from pure Pb^{+2} the pure Sn^{+2}, the bandgap goes through a minimum at about B = $Sn_{0.75}Pb_{0.25}$ with E_g = ~1.2 eV[13-16]. This bandgap tunability enables the realization of two-terminal tandem solar cells which have potential to better utilize the solar spectrum without adding significant additional module costs. HPs can be implemented into a tandem with a mature PV technology with ~1.1eV bandgap (such as c-Si[17] or CIGS[18]) as a runway to commercialization, or HPs with different bandgaps can be utilized together in tandem configuration for a completely solution-processed technology with practically attainable PCE of 32%[19].

Although two-terminal tandem configurations have the greatest possible economic benefit[20], the current matching constraint requires precise bandgap pairings to optimally utilize the solar spectrum, with 1.75eV and 1.82eV having ideal top-cell bandgaps for 1.10eV (c-Si) and 1.22eV (Pb-Sn HP) bottom cells respectively[14]. However, the highest $V_{OC}/V_{OC,SQ}$ reported for a HP in the 1.70-1.85eV bandgap range is ~85%[7, 21], compared to 92% for the lower bandgap HPs[3]. In other words, as the HP bandgap increases from 1.6 to 1.8 eV, the maximum reported V_{OC} remains constant at ~1.24V, suggesting there is no benefit in using a 1.75eV top cell over a thinner 1.6eV top cell. High-bandgap perovskites also suffer from shorter carrier diffusion lengths than the lower E_g alternatives,

which is due to shorter carrier lifetimes (faster non-radiative recombination) as well as lower carrier mobilities[22, 23].

Another concern with the high bandgap HPs is their phase instabilities upon illumination or current injection[24-28]. Hoke *et al.* demonstrated that the I and Br ions redistribute under illumination and form a secondary phase. The photo-excited carriers transfer into the lower bandgap I-rich phase before recombining radiatively as shown by a photoluminescence (PL) peak red-shift upon continuous illumination. This phase segregation is reversible as evidenced by the PL peak position reverting to its original position after the perovskite is left in the dark. Phase segregation has been shown to have adverse effects on device performance,[26] which has been associated with carrier confinement in the low bandgap phase, reducing current collection and attainable ΔE_F[26, 29]. Several groups have reported that high bandgap (FA,Cs)Pb(I,Br)$_3$ HPs are phase stable and have shown stable PL emission and device power output under 1 Sun illumination for modest time periods[11, 22, 23, 30], yet the phase stability of this composition is debated and seems to depend on fabrication route[31, 32]. In addition to phase segregation exhibited by the mixed-halides, HPs have exhibited other forms of instability issues. HPs degrade upon exposure to water or in the simultaneous presence of oxygen and photoexcited or current injected carriers[33-37]. HP devices have further instabilities due to reactions with metal electrodes and some carrier transport layers[17, 38-40]. To achieve the DOE SunShot goal of \$0.03 \$/kWh levelized cost of electricity by 2030, year-over-year degradation rates must be reduced to less than 1%[41].

The perovskite research field has evolved rapidly in the four years of this project. Below we summarize some of the most recent and relevant background from other work.

By the end of 2017, notable advances in high bandgap HP devices and HP stability had been demonstrated:

Large bandgap hybrid perovskites: High bandgap, mixed halide perovskites have been successfully paired with c-Si,[42-45] $Cu_2ZnSn(S,Se)_4$ (CZTS),[46] CIGS,[18, 47] and lead-tin iodide perovskites[48, 49] into monolithic 2-terminal tandems; however, significant voltage losses in mixed halide top cells have prevented such devices from exceeding 80% of their respective detailed-balance limit open circuit voltage[49] (for comparison, the record III-V tandem has a V_{OC} of 2.248 V[50] which is 94.5% of its respective detailed-balance limit). Indeed, the open circuit voltage of single junction mixed halide hybrid perovskites devices with bandgaps between 1.7 and 1.8 eV has not surpassed 1.24 V[51-54] (the detailed balance limit V_{OC} for a 1.75 eV bandgap absorber is 1.463 V).

Observations that V_{OC} does not increase proportionally with increasing bandgap[29, 55-57] and that current decreases with time under constant operation in many mixed halide perovskite devices,[58-60] have driven significant research efforts to discover high bandgap compositions that do not exhibit phase segregation under illumination. Several approaches have been used to suppress the phase segregation that occurs under illumination in high bromide hybrid perovskites including increasing domain size[60], increasing lattice strain,[58] and mixing the A-cation site.[53, 61-64] One effective approach has

been to replace MA with the "double-cation" FA and cesium (FACs), which exhibits a stable PL peak position with time under constant illumination.[22, 53]

A recent review summarizes the current understanding of the light induced phase segregation.[59] Molecular dynamic simulations have predicted phase segregation to be caused by excess charge carriers distorting the lead halide lattice via electron-phonon coupling, while cathodoluminescence experiments studying $MAPb(I,Br)_3$ films before and after light soaking provided evidence that the iodide-rich phase forms mostly between morphological domains during phase segregation.[65]

Perovskite Stability: In order to avoid the degradation pathway induced by light and dry air, the formation of superoxide anion, which is believed to be the main species deprotonating the ammonium groups of organic cations in perovskite[66, 67] was studied. Hague's group[36] discover the generation of superoxide anion is inevitable when perovskite is exposed to light and oxygen. The ab initio simulations based on DFT reveal the transfer of photo-generated electrons to oxygen in defect-free $MAPbI_3$ is energetically favorable (the formation energy is -1.19 eV) since the unoccupied oxygen π^* anti-bonding orbital is located in the middle of the $MAPbI_3$ band gap where it can readily act as an acceptor state for photo-generated electrons. (See figure 25a) The formation energy of superoxide anion is even more favorable (the formation energy is -1.94 eV) when oxygen is located at iodine vacancies in perovskite because the unoccupied oxygen π^* anti-bonding orbital is then shifted down to the position slightly below the conduction band. (See figure 25b) Therefore, reducing iodine vacancies in perovskite can mitigate this degradation pathway.

Since the formation of superoxide anion is inevitable, a different strategy is necessary to stop the degradation pathway triggered by light and dry air: have the deprotonation reaction to reach an equilibrium. A recent publicaiton[38] reports use of sputtering an ITO layer on perovskite PV devices as an electrode and an encapsulant. This sputtered ITO layer served well to prevent the egress of methylamine and other products during the degradation. As a result, the device could maintain its maximum efficiency under the exposure to light and ambient air at room temperature for long periods.

By the end of the project (October 2018), further advances had been demonstrated related to high bandgap perovskite and tandem devices:

Tan *et al.* claim MAI (or other dipolar cations) are important for healing deep trap defects in high bandgap perovskites[68]. Leijtens *et al.* demonstrate a new HP-HP tandem record PCE of 19.1% by fabricating thicker Pb-Sn bottom cell absorber layers and decreasing absorption losses[69]. Zhou *et al.* combine SCN^- exposure with FAI excess to attain V_{OC}s of 1.31V (for 1.93eV bandgap) for n-i-p architecture cells[70]. To improve the p-i-n $V_{OC}/V_{OC.,SQ}$ state-of-the-art, Luo *et al.* used GAI regrowth the attain 1.21V for 1.62eV bandgap, improving interface quality[71]. Finally, Stolterfoht *et al.* find that adding interlayers of PFN and LiF in PTAA/HP/C_{60} architecture improve ΔE_F and device V_{OC} and FF[72]. In summary, we are starting to see other groups utilize similar techniques to understand when absorbers or interfaces are limiting device performance, and we see many groups using similar approaches to improve either HP or interface quality.

Introduction:

In order to achieve the project objective of developing high efficiency tandems that utilize hybrid perovskites, the work plan was broken down into 6 focused tasks over the 4-year planned project duration.

- Task 1: Developing Combinatorial Spray Coating Method for Perovskites. This task was focused on developing methods for depositing a large number of compositions to screen for high optoelectronic quality using our advanced photoluminescence tools.
- Task 2: Developing High-Bandgap Perovskites with High QFLS & Stability. This task focused on using the methods developed in Task 1 to discover high bandgap perovskites with improved optoelectronic quality.
- Task 3: Improving Perovskite Film Morphology. This task focused on improving the film morphology and controlling the phase of promising compositions, including light induced phase segregation in high-bandgap perovskites.
- Task 4: Developing High Bandgap Single Junction Perovskite Solar Cells. This task focused on utilizing the advances of Tasks 1-3 along with interface passivation strategies to yield improved single junction devices with bandgaps and archiectures chosen to utilize for tandems in Task 6.
- Task 5: Developing Interconnect Layers. This task focused on developing high transmissivity low series resistance layers that accept holes from the top cell and electrons from the bottom cell.
- Task 6: Tandem Solar Cells. This task focused on pulling together the advances of tasks 1-5 to yield completed tandem solar cells.

Project Results and Discussion:

Task 1: Develop Combinatorial Spray Coating Method for Hybrid Perovskites

We successfully developed spray coating methods amendable for high-throughput assessment of HP material quality, as shown in Figure 1 and applied is several publications[21, 73]

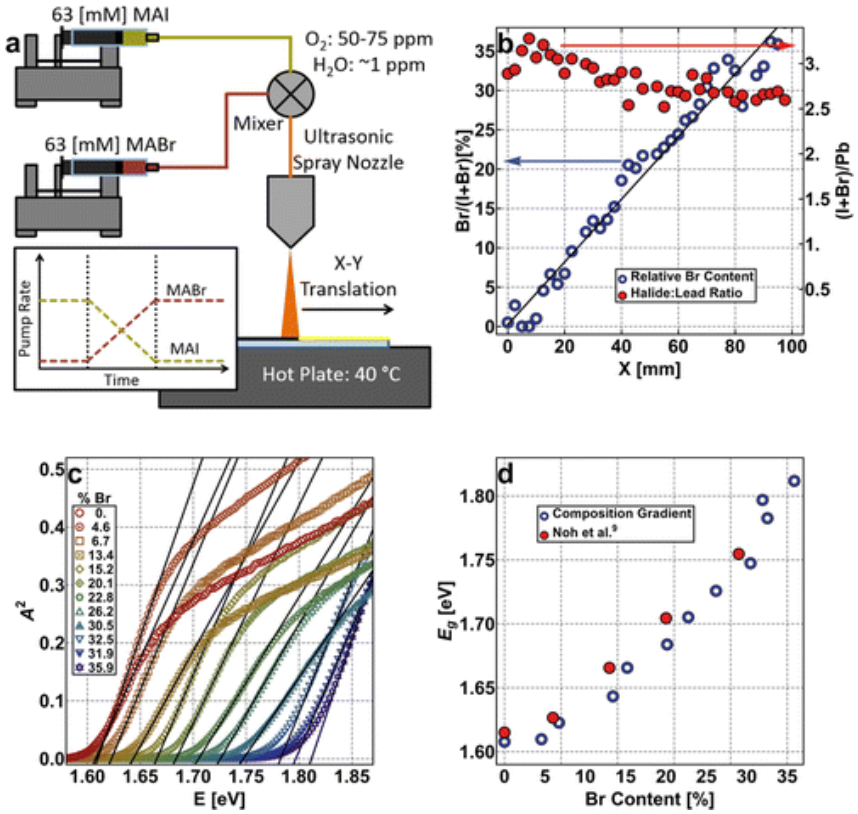

Figure 1. Composition gradient preparation and characterization. (a) Illustration of spray coating setup used to achieve spray gradients. Pumps feed the ultrasonic spray nozzle while it translates across the sample. Inset: pump gantry used, including an initial delay time, pump ramp time and final hold time. (b) EDS results. Relative bromide content (open blue circles) and halide to lead ratio (filled red circles) as a function of distance along the gradient profile as determined by EDS. The black line is to guide the reader's eye. (c) UV−vis−NIR results. Absorbance squared spectra measured at several positions along the gradient with the relative bromide composition of each given in the legend. (d) Extracted bandgap data from linear extrapolation shown as a function of relative bromide content from this work and from Noh et al. using red circles and black squares, respectively.

Task 2: Develop High-Bandgap Hybrid Perovskites with High QFLS & Stability

Subtask 2.1. Mapping the Ternary Halide Composition Space

Here we report optoelectronic quality and stability under illumination of thousands of compositions ranging from the pure iodide (CH3NH3PbI3) to the diiodomonobromide (CH3NH3PbI2Br). Hyperspectral maps of steady-state absolute intensity photoluminescence (AIPL) are used to determine the quasi-Fermi level splitting (QFLS) at each point after synthesis. The QFLS upon first illumination increases with bandgap and reaches a maximum of 1.27 eV under 1 sun illumination intensity for a bandgap of

1.75 eV. However, the optoelectronic quality (χ), defined as the ratio of the QFLS to the maximum theoretical QFLS for bandgap, decreases with bandgap from around 88% for 1.60 eV bandgap down to 82% for 1.84 eV bandgap. Further, we show that a reversible light induced defect forms that reduces the optoelectronic quality, particularly for high-bandgap materials. Even with the light-induced defect, a stable QFLS of about 1.17 eV is possible. Comparing our QFLS to Voc values from HP devices reported in the literature indicates that higher open circuit voltages are possible but may require optimization of band alignment. Further, the spectral shape of the PL emission is found to be more commensurate with Franz–Keldysh broadening from local electric fields or from a screened Thomas–Fermi density of states (as opposed to a joint density of states

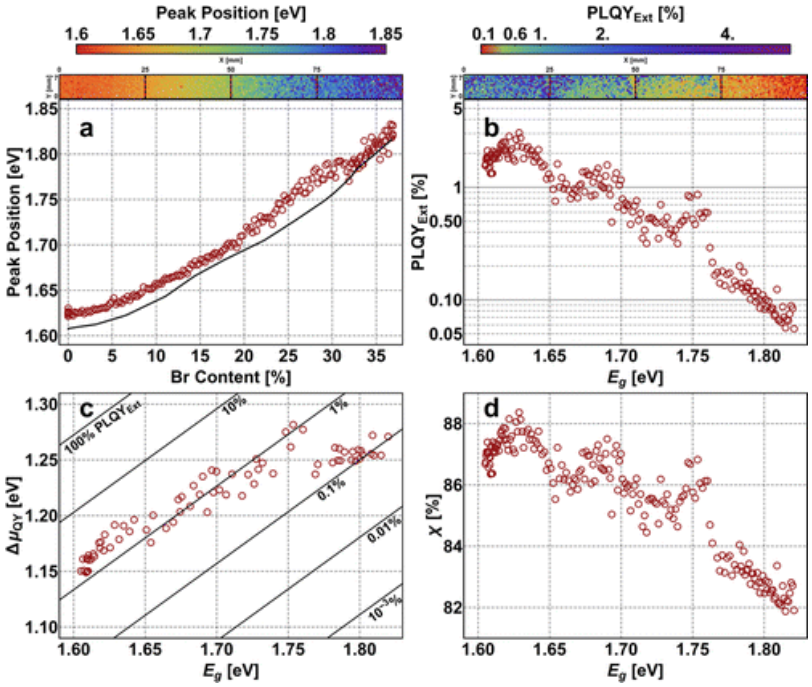

Figure 2. AIPL collected at 1 sun of composition spread library. (a) Spatial map of local peak position with color scale given above. *Y*-position averaged peak position as a function of Br content, with the black line representing the UV–vis determined bandgap trend. (b) Spatial map of local external photoluminescence quantum yield ($PLQY_{Ext}$) with log-scale color bar given above. *Y*-position averaged $PLQY_{Ext}$ given as a function of bandgap. (c) Quasi-Fermi-level splitting determined from PLQY, $\Delta\mu_{QY}$, given as a function of bandgap with black lines representing lines of constant PLQY assuming a lattice temperature of 350 K. (d) Optoelectronic quality parameter, χ calculated as a percent from $\Delta\mu_{QY}/\Delta\mu_{max}$ given as a function of bandgap.

Figure 2 shows milestone M2.1.4 is achieved with this composition range – we measure quasi Fermi-level splitting values between 1.15 and 1.27 eV in the tandem-relevant bandgap regime, which spans 82-88% of the detailed balance limit quasi Fermi-level splitting[73].

Subtask 2.2 Revealing the Role of Hydrogen Bonding

(a) Strain Management in High Bandgap Perovskites through Combinatorial Spray Coating

We study the impact of A^+ size mismatch induced lattice distortions (in ABX_3 structure) on the optoelectronic quality of high-bandgap HPs and find that the highest quality films have high A-site size-mismatch, where large guanidinium (GA) compensates for small Cs to keep the tolerance factor in the range for the perovskite structure (see Figure 3). Specifically, we find that 1.84eV bandgap $(FA_{0.33}GA_{0.19}Cs_{0.47})Pb(I_{0.66}Br_{0.34})_3$ and 1.75eV bandgap $(FA_{0.58}GA_{0.10}Cs_{0.32})Pb(I_{0.73}Br_{0.27})_3$ attain quasi-Fermi level splitting of 1.43eV and 1.35eV, respectively, which is >91% of the Shockley-Queisser limit for both cases. Films of 1.75eV bandgap $(FA,GA,Cs)Pb(I,Br)_3$ are then used to fabricate p-i-n

photovoltaic devices that have a V_{OC} of 1.24 V. This V_{OC} is among the highest V_{OC} reported for any HPs with similar bandgap (1.7 to 1.8 eV) and a substantial improvement for the p-i-n architecture, which is desirable for tandems with Si, CIGS, or a low-bandgap HP. Collectively, our results show that non-radiative recombination rates

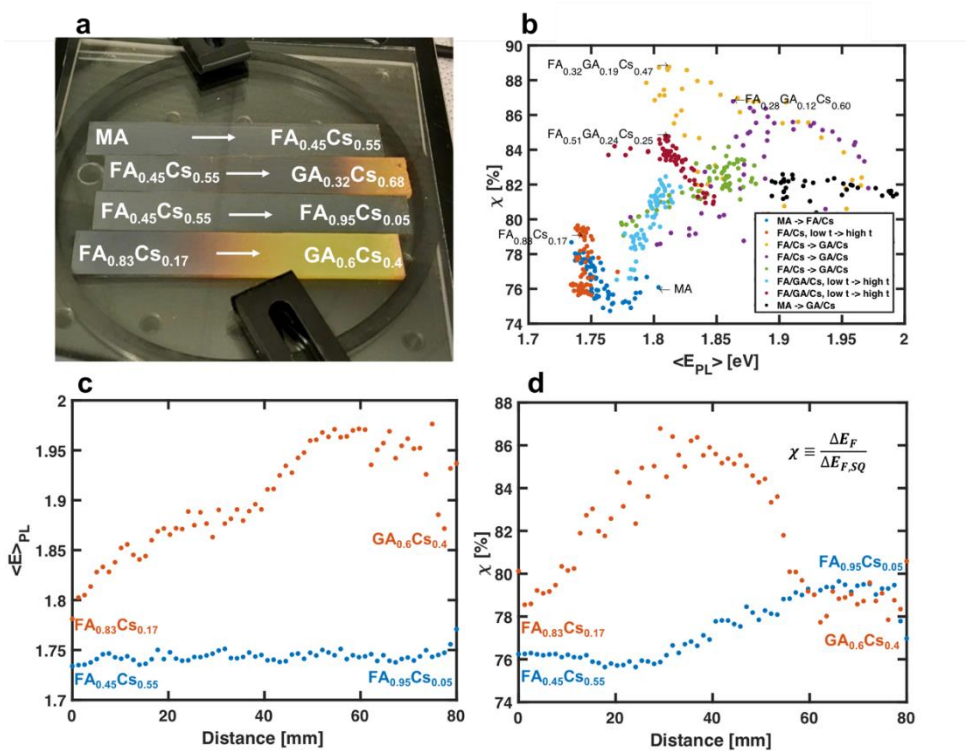

Figure 3. Spray coated A-site composition gradients of HPs and their optoelectronic quality for a fixed iodide to bromide ratio, or $APb(I_{0.66}Br_{.34})_3$, where A can be an alloy containing FA, MA, GA, or Cs. (a) Photo of four example gradients; composition along the 80 mm substrate is a linear combination of the compositions listed on the ends. Samples are enclosed behind two glass sheets with a quartz top window using an O-ring, vacuum grease, and clamps screwed into an optical stage to ensure AIPL measurements are collected with the samples in a N_2 environment. (b) Compiled AIPL results for eight gradients, showing optoelectronic quality fraction χ vs. mean PL emission energy, with several compositions of interest highlighted. Note that $\Delta E_{F,SQ}$ is identical to $qV_{oc,SQ}$. (c-d) example results showing (c) mean PL emission energy and (d) optoelectronic quality as the composition changes along the length of the gradient for two example gradients. Note that the absolute intensity PL measurements were collected at 1 Sun photon flux (541 W/m^2 with a 532nm cw laser)

are reduced in $(FA,GA,Cs)Pb(I,Br)_3$ films and prove that FA-GA-Cs alloying is a viable route to attain high V_{OC} in high-bandgap HP solar cells[74].

(b) Correlation between Photoluminescence and Carrier Transport and a Simple In Situ Passivation Method for High-Bandgap Hybrid Perovskites

Several recent developments have confirmed that enhancing crystallinity and increasing lattice strain are both successful in reducing phase segregation in mixed-halide perovskites, creating films that show phase stability under 1 Sun illumination[22, 53, 54]. However, in the few cases demonstrating phase stable materials, the voltage deficit is still much greater in the high bandgap perovskites than their low bandgap (~1.6eV) predecessors, and diffusion lengths are too low for optically thick current matched

devices. Photoluminescence can be used to rapidly screen material optoelectronic quality to explore methods to reduce the voltage deficit in high bandgap perovskites. However, studying photoluminescence alone to characterize overall optoelectronic quality has some potential pitfalls as alone it does not provide information on carrier transport, which may affect the recombination process by localizing carriers. While photobrightening has been observed in perovskites under several situations including low-light exposure (trap filling)[75] treatment with Lewis bases (defect passivation)[76, 77] or during aging in air[78, 79], it is unclear if the PL enhancement is due to a reduction or passivation of non-radiative recombination centers in the bulk or due to spatial confinement of carriers. Quantifying carrier transport by measuring the effective diffusion length simultaneously with photoluminescence would reveal the coupling (or lack thereof) between transport and recombination and provide a clearer understanding of the optoelectronic properties of HPs along with a means to assess material stability and defect passivation efforts. Here, we use a photoconductivity-based method to estimate the average carrier diffusion length coupled simultaneously with absolute intensity PL measurements. ***We show for the first time that there is an intimate (and sometimes dramatic) correlation between carrier transport and photoluminescence*** (see Figure 4). We also show a new a and simple in-situ method to increasing passivation in HP films. In this work, we also assess the role of A^+ cation and surface passivation on PL-L_D behavior.

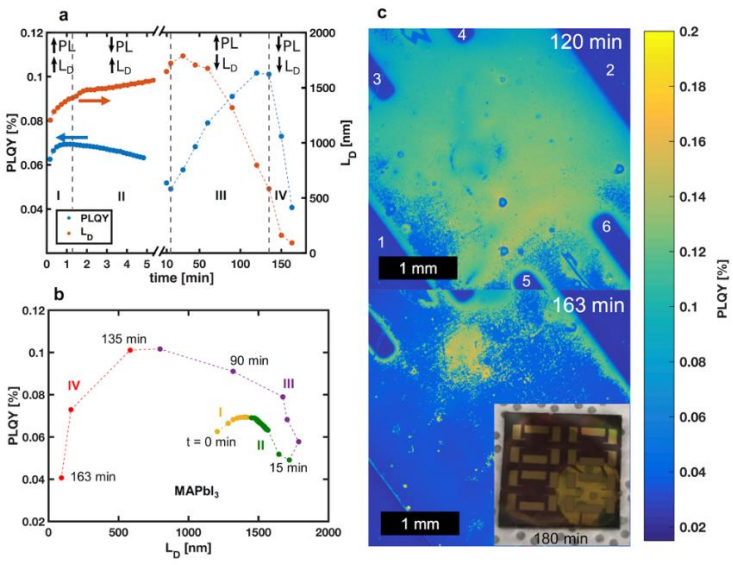

Figure 4. Correlation between photoluminescence quantum yield and mean carrier diffusion length as a function of time for $MAPbI_3$ degradation in air (35% RH) under steady 1 Sun illumination. (a) The PLQY and L_D plotted each with time for 1.61 eV bandgap $MAPbI_3$ at effective 1 Sun illumination with a calibrated blue LED. Ideal stable behavior would appear as straight horizontal lines. However, several distinct regimes of change and correlation are observed (I, II, III, and IV). Note region III where significant photobrightening is observed simultaneously with loss of diffusion length. (b) Same data as in part (a) but plotted together (PLQY vs. L_D) parametrically with time. Ideal stable behavior would be a stationary point. (c) Wide-field PL images at 120 min and 163 min during the $MAPbI_3$ degradation. Au contacts are labeled in the "120 min" PL image. (c, inset) Photo of $MAPbI_3$ film after exposure to air and 1 Sun excitation for three hours.

Subtask 2.3 Development of Lead-free Hybrid Perovskites

In Year 1, we explored divalent cations such as tin (II), germanium (II), and copper (II). Both partial lead replacement and total substitution were characterized with a variety of halide compositions. The methylammonium organic cation was used in all cases to simplify the combinatorial studies determining the compositional space in which the hybrid perovskite lattice can be maintained. Our initial work shows that the only serious

elemental candidate for Pb substitution is Sn. Thus, in our continuing effort to replace Pb, Pb-Sn alloys will be the primary system of study.

(a) Lead-Tin Hybrid Perovskites

We employed a combined compositional, process, and interfacial engineering to develop highly efficient and stable Pb-Sn binary perovskite solar cells with successful Pb replacement up to 25%. By adopting solvent-washing methodology, homogeneous and densely crystalline $MA_{1-y}FA_yPb_{1-x}Sn_xI_3$ films could be attained. The energy levels of these resultant binary perovskites were carefully investigated to facilitate the selection of appropriate CTLs for minimizing recombination losses and maximizing charge transfer efficiency of the derived devices. Due to the improved morphology of low E_g $MAPb_{0.75}Sn_{0.25}I_3$ and carefully chosen CTLs, the derived PVSC showed an impressive PCE of 14.35%. More importantly, the tendency of easy Sn^{2+} oxidation could be alleviated by incorporating FA cations to form a low E_g (1.33 eV) mixed-cation Sn-based perovskite, $MA_{0.5}FA_{0.5}Pb_{0.75}Sn_{0.25}I_3$. As a result, a PVSC with a stabilized PCE of 14.19% can be achieved. $MA_{0.5}FA_{0.5}Pb_{0.75}Sn_{0.25}I_3$ PVSC exhibited an improved J_{SC} (23.03 mA cm^{-2}) compared to that of $MAPb_{0.75}Sn_{0.25}I_3$ device due to a slightly smaller E_g. Moreover, 80% and 94% of initial PCE can be retained after 12- and 30-day storage in ambient (30-40% RH) and inert atmospheres, respectively. The implications of this work coupled with further compositional engineering would be vital to fuel the development of Pb-free large E_g PVSCs.

We found that the introduction of Cs effectively modulates the film formation of Pb–Sn perovskites and thus results in improved film quality for high Sn-containing compositions. This is attributed to the reduced crystallization rate in the presence of Cs cations. As a result, both $MAPb_{1-x}Sn_xI_3$ and $FAPb_{1-x}Sn_xI_3$ PVSCs with high Sn substitution ratios can deliver enhanced PCE and stability with an appropriate amount of Cs incorporation (Figure 5a-b). For instance, with 50% Sn, $MA_{0.9}Cs_{0.1}Pb_{0.5}Sn_{0.5}I_3$ and $FA_{0.8}Cs_{0.2}Pb_{0.5}Sn_{0.5}I_3$ perovskites possess a low E_g of 1.26–1.28 eV and afford high PCEs of 10.07% and 11.63%, respectively, outperforming the performance of the PVSCs without Cs. More importantly, the $MA_{0.9}Cs_{0.1}Pb_{0.5}Sn_{0.5}I_3$ based device can maintain ~75% of its initial PCE after being annealed at 85 °C under inert conditions for 12 days and ~76% of its initial PCE after being stored in an ambient environment with a relative humidity of 35% for 20 days (Figure 14c-d).

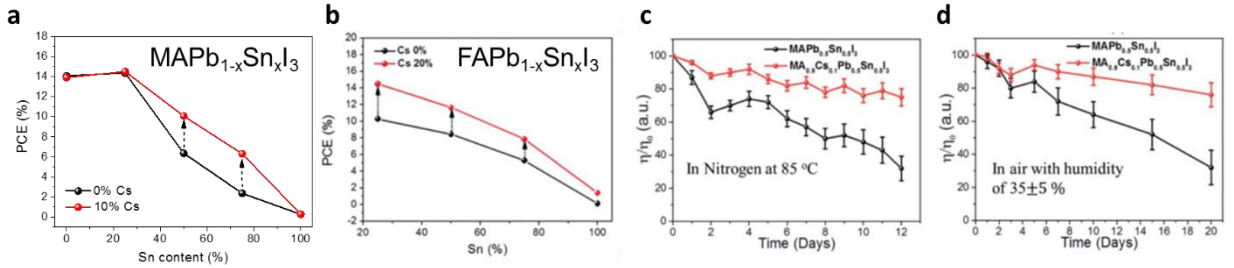

Figure 5. (a) Performance comparison of $MAPb_{1-x}Sn_xI_3$ and $MA_{0.9}Cs_{0.1}Pb_{1-x}Sn_xI_3$ PVSCs. (b) Performance comparison of $FAPb_{1-x}Sn_xI_3$ and $FA_{0.8}Cs_{0.2}Pb_{1-x}Sn_xI_3$ PVSCs. (c) Thermal stability and (d) ambient stability test of $MAPb_{1-x}Sn_xI_3$ and $MA_{0.9}Cs_{0.1}Pb_{1-x}Sn_xI_3$ PVSCs.

With optimized processing conditions and additive formulation, a phase pure $MAPb_{0.5}Sn_{0.5}I_3$ film was obtained with homogenous coverage and excellent crystallinity

with an E_g of 1.22 eV. There is a significant mismatch between conduction band minimum of $MAPb_{0.5}Sn_{0.5}I_3$ and the lowest unoccupied molecular orbital of C_{60}. The difference in energy levels can be reduced by using an alternate fullerene variant, Indene-C60 bis-adduct ($IC_{60}BA$) as ETL (**Figure 6a**). Relatively small PLQY and faster PL decay illustrate dominance of nonradiative losses on charge transfer at the $MAPb_{0.5}Sn_{0.5}I_3/C_{60}$ interface, which ultimately constrained device performance. With $IC_{60}BA$ we not only mitigate hysteresis related instability but also realize a remarkably high V_{oc} (0.84 V), which is ≈88% of the SQ limit (**Figure 6b-f**). Stable devices with small $V_{oc,loss}$ (≈0.38 V) realized here is the lowest among reported Pb-Sn binary PVSCs. This provides a platform to realize high V_{oc} in 2-T tandems. These results have been published as a part of an article in Advanced Materials[14].

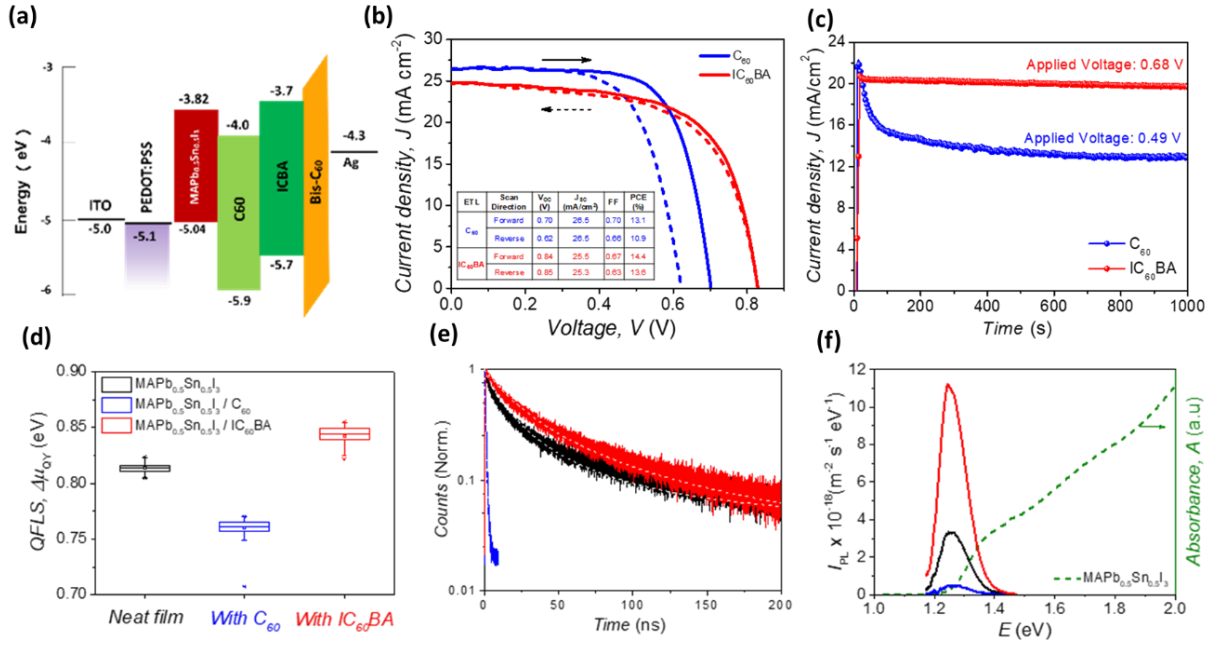

Figure 6. Photovoltaic and optoelectronic characteristics of Pb-Sn binary alloys. (a) Energy level diagram. (b) Typical *J-V* characteristics. (c) steady-state current under AM1.5 illumination at an applied voltage corresponding to MPP. (d) Quasi-Fermi level splitting values. (e) Transient photoluminescence. (f) photoluminescence spectra.

Our previous work has demonstrated a greatly improved PCE and stability of Pb-Sn PVSCs using a combined process, interfacial, and compositional engineering[14]. Such binary alloy compositions provide a platform for development of ideal bandgap (1.3-1.4 eV) absorbers, pivotal to further improve PCE of single junction PVSCs because of better balance between absorption loss and thermalization loss as demonstrated by Shockley-Queisser detailed balanced calculation. However, ideal bandgap PVSCs are currently hindered by poor optoelectronic quality of perovskite absorbers and their PCEs have stagnated at <15%[80]. We systematically investigated the optoelectronic properties of $MAPb_{1-x}Sn_xI_3$ alloys to find the origin of stagnation in developing ideal bandgap Pb-Sn alloys and identify that currently used 75%Pb-25%Sn alloy is intrinsically defective.

Subsequently, we have rationally developed an ideal bandgap perovskite composition ($MAPb_{0.5}Sn_{0.5}(I_{0.8}Br_{0.2})_3$) and show its superiority to $MAPb_{0.75}Sn_{0.25}I_3$. To fabricate efficient solar cells using the developed ideal bandgap perovskite absorber, we chose PEDOT:PSS and doped-ICBA as HTL and ETL respectively (**Figure 7a**). The comparison of two different ideal bandgap compositions clearly portrays the merits of improved optoelectronic properties (lower non-radiative recombination losses and higher absorption coefficient) of $MAPb_{0.5}Sn_{0.5}(I_{0.8}Br_{0.2})_3$ in realizing high performance (**Figure 7b-c**). As the thickness of perovskite increased, the V_{OC} and FF were maintained and the J_{SC} increased from 21.51 to 25.67 mA cm^{-2}, resulting in a **PCE increase from 14.71 to 17.13%**; the relatively unchanged V_{OC} and *FF* demonstrates excellent optoelectronic quality of the newly developed composition, which is not limited by charge transport within the perovskite layer (**Figure 7d-f**). PCE > 15% achieved here surpasses requirements of **Milestone 2.3.5**. These results were published in Advanced Materials[81].

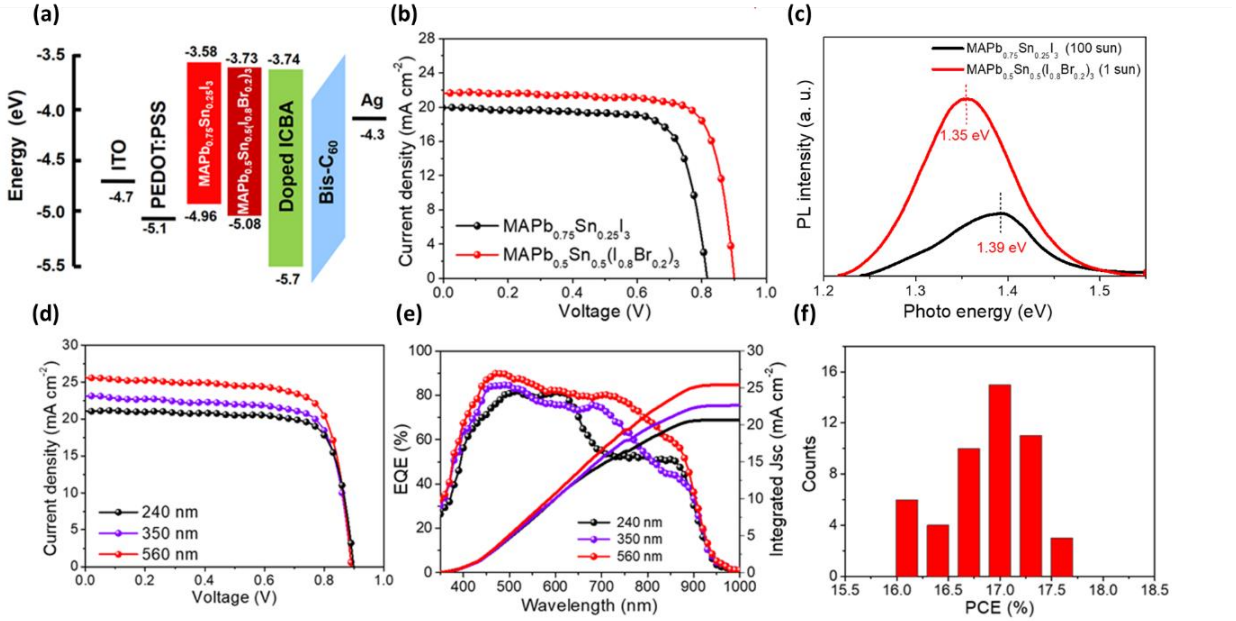

Figure 7. Photovoltaic and optoelectronic characteristics of ideal bandgap PVSCs. (a) Energy level diagram. (b) Typical *J-V* characteristics under AM 1.5 illumination and (c) PL spectra of $MAPb_{0.75}Sn_{0.25}I_3$ and $MAPb_{0.5}Sn_{0.5}(I_{0.8}Br_{0.2})_3$ perovskite with same film thickness of 240 nm. (d) Typical *J-V* characteristics and (e) EQE spectra of $MAPb_{0.5}Sn_{0.5}(I_{0.8}Br_{0.2})_3$ PVSCs with different perovskite thicknesses of 240, 350, and 560 nm. (f) Efficiency distribution of the optimized $MAPb_{0.5}Sn_{0.5}(I_{0.8}Br_{0.2})_3$ PVSCs.

(c) Pure Tin Perovskites

Besides the regular 1-step deposition, sequential deposition route (generally denoted as 2-step deposition) has also been widely used for preparing the Pb-based perovskites and been shown to afford good quality control of the deposited film. Recently, 2-step method has been reported via thermal evaporating SnI2 with FAI film, and this perovskite layer based device showed 3.98% PCE on indium tin oxide (ITO) substrate and 3.12% PCE on flexible substrate[82]. However, the 2-step deposition has not been fully explored so far for

depositing the Sn-based perovskites due to fast reaction of precursors as discussed earlier. Different from the 1-step deposition, where the evolution of perovskite crystallization mainly encompasses film shrinkage, the 2-step deposition involves additional volume expansion of precursory PbI_2/SnI_2 film before the intercalations with MAI/FAI precursors. Recently, the evolved intermediate phase based on iodoplumbate anions that mediates the perovskite crystallization has been embodied as the Lewis acid–base adduct formed by metal halides (serve as Lewis acid) and polar aprotic solvents (serve as Lewis base[83]). Based on this principle, we propose to constitute efficient Lewis acid–base adduct in the SnI_2 deposition step to modulate its volume expansion and fast reaction with MAI/FAI (FAI is studied hereafter). Herein, trimethylamine (TMA) is employed as the additional Lewis base in the tin halide solution to form SnY_2–TMA complexes (Y = I−, F−) in the first-step deposition, followed by intercalating with FAI to convert into $FASnI_3$. We showed that TMA can facilitate the homogeneous film formation of SnI_2 (+SnF_2) layer by effectively forming the intermediate SnY_2–TMA complexes (**Figure 8a**). Meanwhile, its relatively larger size and weaker affinity with SnI_2 than FA^+ ions will facilitate the intramolecular exchange with FA^+ ions, thereby enabling the formation of dense and compact FASnI3 film with large crystalline domain (>1 µm). As a result, high PCEs of 4.34% and 7.09% with decent stability were successfully accomplished in both conventional and inverted PVSCs (**Figure 8b, c**), respectively, comparable to the state-of-the-art values reported in the literature. This work has been published in *Advanced Materials*[84].

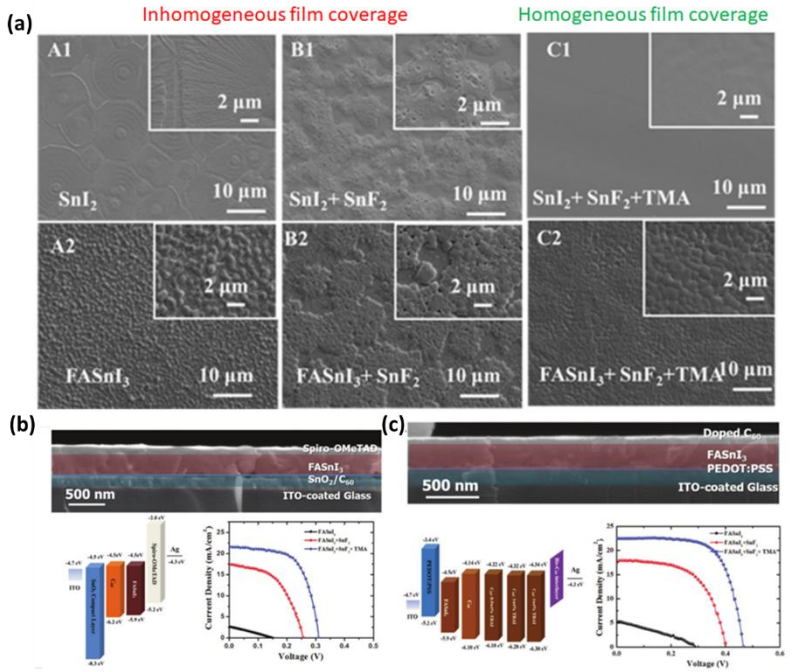

Figure 8. (a) SEM images of: A1,A2) SnI_2 and $FASnI_3$, B1,B2) SnI_2+SnF_2 and $FASnI_3$+SnF_2, and C1,C2) SnI_2+SnF_2+TMA and $FASnI_3$+SnF_2+TMA perovskite films fabricated by the two-step method. Cross-sectional SEM image, energy level diagram and J-V curves of the fabricated PVSCs based on (b) conventional and (c) inverted device architectures.

Task 3: Hybrid Perovskite Film Morphology

Here, we have developed three facile methods to modulate the crystallinity and surface morphology of solution-processed polycrystalline perovskite thin films to effectively enhance the resulting photovoltaic performance of the derived solar cells. ***Milestone 3.2 related to improved morphology by additive is met in this section***.

(a) Roles of Alkyl Halide Additives in Enhancing Perovskite Solar Cell Performance

Alkyl halides with different alkyl chain lengths and end-groups have been systematically investigated to elucidate their influence on the performance of perovskite solar cells, as shown in **Figure 9a**. All the studied additives have resulted in clearly enhanced crystallization and substrate coverage in solution-processed perovskite thin films. As a result, PCE of devices made from these additive-enhanced perovskites increase from 9.8% (based on pristine perovskite) to as high as 13.1%. More interestingly, we found out that the characteristic peaks in XRD pattern, the absorption band-edge in UV spectra, and the resultant color (**Figure 9b**) of the thin film processed from MACl + $PbCl_2$ + 1,4-diiodobutane (1,4-DIB) formula are almost identical to that of conventional $CH_3NH_3PbI_{3-x}Cl_x$ (processed from 3MAI + $PbCl_2$). All these results indicate that the thin-film processed form the new formula can result in the formation of $CH_3NH_3PbI_{3-x}Cl_x$. Since 1,4-DIB is the only source for iodide, this result obviously demonstrates that the C-I bond in 1,4-DIB was cleaved and the resulting iodide participated in the crystallization process of perovskite. All these discoveries enables us to conclude that the observed change of crystallization dynamics induced by alkyl halides should be the cooperative results of modulated solvent-solute interactions between alkyl halides and Pb^{2+} as well as the cleaved C-I bond during thermal annealing, as is illustrated in **Figure 9c**. These combined findings prove that alkyl halide additives can play multiple roles in modulating the dynamics of perovskite crystal growth. As a result, all the studied additives enhance crystallization and surface coverage of solution-processed perovskite thin films and enable significantly enhanced PCE (from 9.8% in device made from a pristine perovskite to as high as 13.1% in additive-processed perovskites) (**Figure 9d**). Our study opens up new perspective on perovskite preparation to for optimizing perovskite active layer properties to expand device performance ceilings.

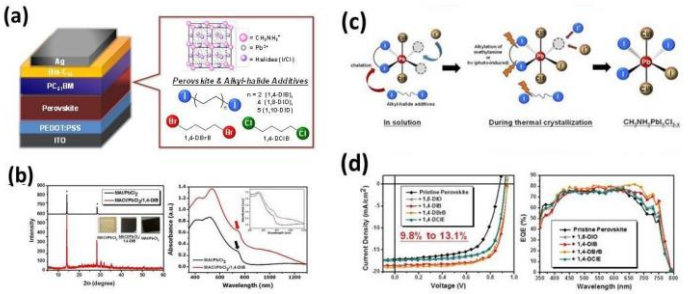

Figure 9. (a) The configuration of PHJ device and the studied alkyl halide additives. (b) Comparison of XRD and UV-vis of the perovskite thin films processed from 3MAI+$PbCl_2$ (mole ratio: 3:1, 40 wt%) and MACl+$PbCl_2$+1,4-DIB (mole ratio: 1:1:4, 11.4 wt%). The insert are the real pictures of the perovskite thin films, processed from different precursor solutions, after thermal annealing at 90 ^oC. (c) Illustration of the roles of alkyl-halide additives during perovskite crystallization. (d) *J-V* curves and EQE spectra of the best studied PHJ solar cells under 100 mW cm^{-2} AM1.5 illumination.

(b) Fast MA Vapor Treatment

Here, we describe a fast (less than 1s) and simple post deposition chemical treatment in which crystal reconstruction induced by a methylamine (MA^0) vapor greatly improves perovskite film coverage, crystallinity, and device performance (**Figure 10**). We not only demonstrate the efficacy of this chemical treatment in improving the photovoltaic performance of a PHJ device, we also mechanistically study the process to reveal the role of hydrogen bonding between methylamine vapor and the perovskite's organic sublattice in mediating the material's reactivity toward the vapor through the exploration of a variety of hybrid perovskite systems. Furthermore, through detailed microscopy, we

also demonstrate that the nature of MA^0-perovskite coordination and its microstructural consequences are a function of MA^0 vapor pressure, interaction time, and composition of the organic sublattice. Ultimately, we offer design rules for amine vapor based hybrid perovskite post chemical treatments (**Figure 11**).

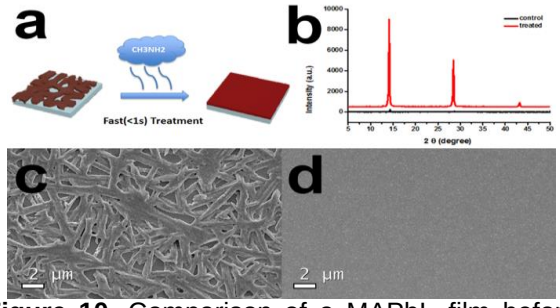

Figure 10. Comparison of a $MAPbI_3$ film before and after the vapor process depicted in (a): (b) XRD of a sample before vapor exposure (control) and immediately after vapor exposure at room temperature (treated). SEM images before vapor exposure (c) and immediately after vapor exposure at room temperature (d).

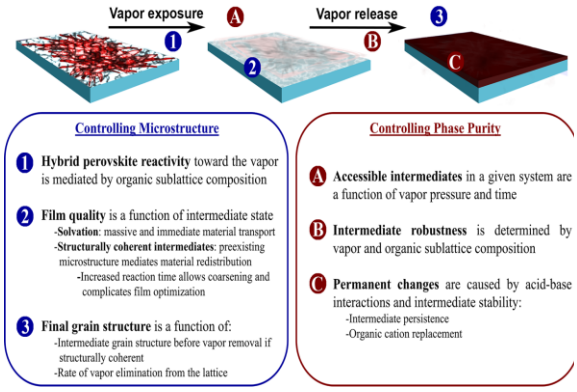

Figure 11. Design rules for MA^0 vapor based post deposition treatments for organo-metal halide perovskites in general.

(c) Fluoroalkyl-substituted fullerene/perovskite heterojunction (FPHJ) for efficient and ambient stable perovskite solar cells

To mitigate the adverse effects caused by defects and improve stability in parallel, we developed a fluoroalkyl-substituted fullerene, DF-C_{60} to form a f-FPHJ and demonstrated its potential to realize efficient and ambient stable PVSC. The DF-C_{60} was directly added into perovskite solution with appropriate weight ratio (0.01-0.1 wt%) to formulate f-FPHJ. The surface morphology of the prepared f-FPHJ films with different blending concentrations of DF-C_{60} showed that the grain size increased from 100-200nm to 300-400 nm for f-FPHJ films. Such increase in grain size might be because the DF-C60 can move around to reduce compressive stress induced by the volume expansion during film evolution while it can also fill the spaces left in the entire film. However, as at 0.1 wt% pinholes start to appear in film which can be attributed to phase separation between $MAPbI_3$ and DF-C60. As the loading of DF-C60 increased, more white spots are observed at the GBs indicating aggregation of DF-C60 given that no clear secondary phase is observed in XRD. This supports that the blended fullerene tends to distribute at the GBs of the perovskite films as reported in literature.[85] Like the previously reported FPHJs,[86, 87] the DF-C60 is proven to effectively passivate the defects in the perovskite film to facilitate the charge transport/collection in the derived PVSC (Figure 12a-f). Consequently, the f-FPHJ device can ***yield an enhanced PCE of 18.11%, outperforming that of the pristine $CH_3NH_3PbI_3$ device (15.67%)*** (Figure 12g-f). Finally, benefitting from the hydrophobicity of DF-C60, the un-encapsulated f-FPHJ device shows better stability against moisture than that of the pristine device. More than 83% of the initial PCE can be retained after being stored in ambient with a relative humidity of 60 ±5% for 1 month while the PCE of the pristine device degraded to lower than 22% of its initial value after stored under the same environment for 22 days. The realization of 18.11 % PCE in this work

directly fulfills the Go/No-Go 6 (option 1), which requires demonstration of an 18% PCE single junction HP solar cell without constraints.

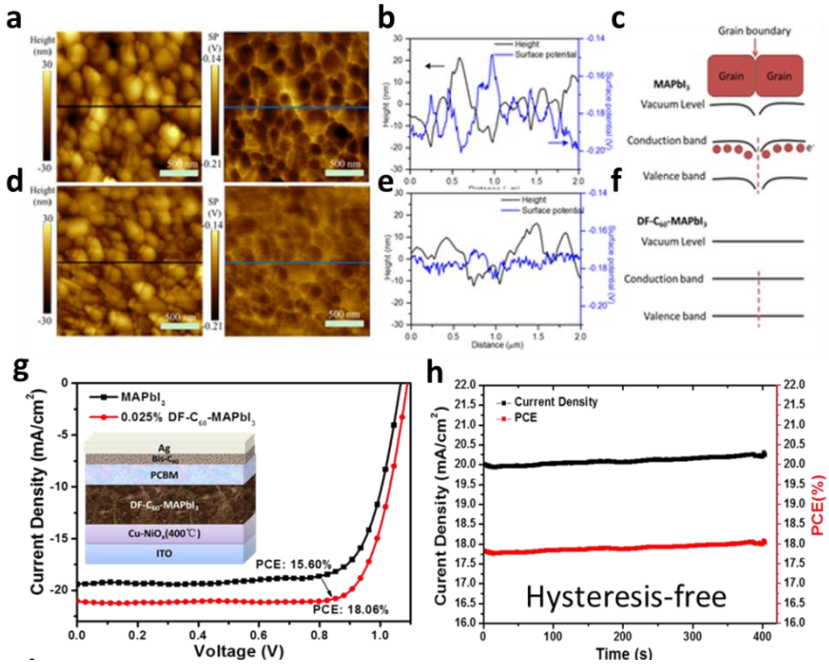

Figure 12. (a, d) height and work function channel's pictures, (b, e) value of work function obtained using scanning kelvin probe microscopy, and (c, f) scheme of energy bending and alignment at GBs for the pristine MAPbI3 (top) and 0.025 wt% DF-C60-MAPbI3 (bottom) films, respectively. (g) J-V curves, (h) the stabilized Jsc and PCE of 0.025 wt% DF-C60-MAPbI3 devices.

(d) Role of Grain Size in Current-Induced Phase Segregation in Mixed Halide Hybrid Perovskites and its Impact on Two-Terminal Tandem Solar Cell Design

We investigate the origin of phase segregation and implication for tandems with mixed halide large-bandgap (~1.75 eV) perovskites. We show explicitly that $MAPb(I_{0.6}Br_{0.4})_3$ and $(MA_{0.9},Cs_{0.1})Pb(I_{0.6},Br_{0.4})_3$, termed "MA" and "MACs", respectively, rapidly phase segregate in the dark upon 1 sun equivalent current injection. This is direct experimental evidence that conduction band electrons or valence band holes are the culprit behind phase segregation. In contrast, $(FA_{0.83},Cs_{0.17})Pb(I_{0.66},Br_{0.34})_3$, or "FACs," prepared at only 75 °C resists phase segregation below 4 sun injection. FACs prepared at 165 °C yields larger grains and withstands higher injected carrier concentrations before phase segregation (Figure 13). The FACs and

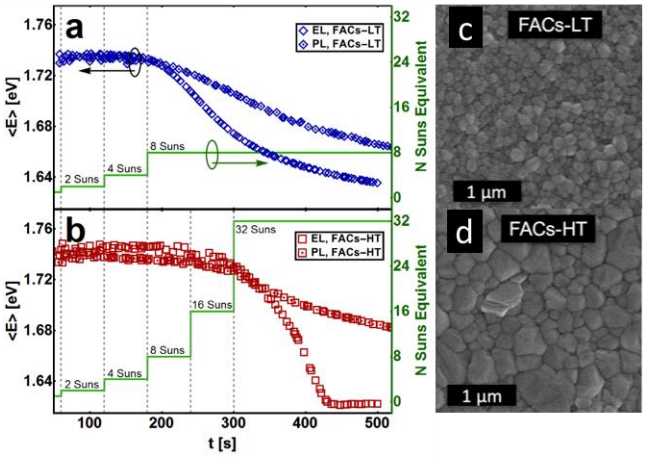

Figure 12. Mean emission spectrum energy with time. The electroluminescence current density and photoluminescence illumination intensity is doubled every minute. Results are shown for (a) Low temperature and (b) high temperature annealed $(FA_{0.83},Cs_{0.17})Pb(I_{0.66}Br_{0.34})_3$. SEM micrograhs are shown in (c) and (d).

MACs devices sustain near constant power output at 1 sun and do not affect the current output of a CIGS bottom cell when used as an incident light filter[88].

Task 4: Develop High Bandgap Single Junction Hybrid Perovskite Solar Cells

Subtask 4.1. Interface Engineering of the ETM, HTM and Passivation Layer

(a) CuSCN as an HTM

Herein, we are particularly interested in demonstrating a high performance PHJ HPSC using solution-processed CuSCN HTL. By utilizing diethylsulfide (DES), which has higher solubility (>40 mg/mL) and low boiling point (ca. 90 ˚C) than dipropylsulfide (~20 mg/mL and ca. 140 ˚C), as the processing solvent for CuSCN,[89] a very thin and compact film can be easily obtained by simple spin-coating technique. Its good resistance to polar solvents (such as DMSO) can serve as a robust underlying layer to allow the subsequent solution processing of PHJ HPSCs. Moreover, CuSCN shows much higher transmittance than PEDOT:PSS in the entire UV-Vis-NIR range, and especially in the NIR, which is crucial for the development of monolithic tandems where the perovskite is the top cell. The CuSCN films show superior transmittance in the Vis-NIR as their thicknesses were increased from 25 to 150 nm. ***Figure 14a*** presents the *J–V* curves of fabricated HPSCs based on CuSCN with different thickness and the reference device based on PEDOT:PSS. Encouragingly, the optimized CuSCN-derived HPSC (CuSCN thickness: 40 nm) exhibited an impressive PCE_{MAX} of 16% while the control PEDOT:PSS-based device only yielded a 12.1% PCE_{MAX}. The major improvement lies on the increased V_{OC} (from 0.91 V to 1.07 V). It is noteworthy that the morphology and crystallinity of $MAPbI_3$ layers on both CuSCN and PEDOT:PSS HTLs were quite similar, indicating the improved V_{OC} of the CuSCN-based device relative to PEDOT:PSS-based device is mainly attributed to the better energy level matching at the CuSCN/perovskite interface than the PEDOT:PSS/perovskite. In addition to the V_{OC}, J_{SC} (18.4 mA/cm^2 to 19.8 mA/cm^2) and FF (0.72 to 0.76) were also slightly improved in the CuSCN-based devices. The enhanced J_{SC} and FF can be interpreted as the consequence of more efficient hole extraction and electron blocking of CuSCN than PEDOT:PSS. Note that the high transmittance of CuSCN is another important reason for the improved J_{SC} of devices. More importantly, the CuSCN-based device can possess an improved device stability than the PEDOT:PSS-based one, as shown in ***Figure 14b***.

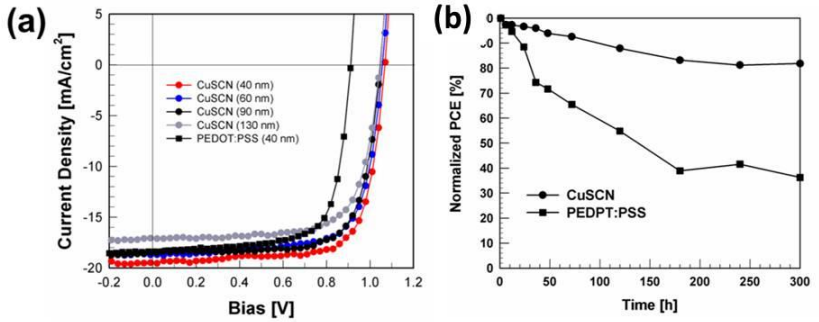

Figure 14. (a) J−V curves with different thickness of CuSCN as compared to the PEDOT:PSS under AM1.5G illumination, and (b) the ambient device stability of the optimized HPSCs with CuSCN or PEDOT:PSS, measured periodically but not kept under constant illumination.

(b) Roles of Fullerene-based ETLs in Enhancing the Performance of HPSCs

Herein, we demonstrate a clear correlation between the charge-transporting properties of fullerene-based ETLs and photovoltaic performance by systematically studying three fullerenes, $IC_{60}BA$, $PC_{61}BM$, and C_{60} (***Figure 15***). We first verified the electron mobility of the studied fullerenes by field-effect transistors (FETs). The electron mobility gradually increases from $IC_{60}BA$ (6.9×10^{-3} cm^2/Vs), to $PC_{61}BM$ (6.1×10^{-2} cm^2/Vs), to C_{60} (1.6 cm^2/Vs) due to the increased conjugation of fullerene core. To elucidate the influence of electron mobility of fullerene-based ETLs on the photovoltaic performance of HPSCs, a conventional device configuration of ITO/PEDOT:PSS (35-40 nm) / $MAPbI_3$ (300 nm) / fullerenes (~60 nm)/Bis-C_{60} (10 nm)/Ag (150 nm) was fabricated.[90-93] All the fullerene ETLs are spin-cast for fair comparison. Impressively, the C_{60}-based device afforded the highest PCE_{MAX} of 15.44% with a V_{OC} of 0.92 V, a J_{SC} of 21.07 mA/cm^2, and a FF of 0.80. The $PC_{61}BM$- and $IC_{60}BA$-based devices showed PCEs of 13.37% (V_{OC}: 0.89 V, J_{SC}: 18.85 mA/cm^2, and FF: 0.80) and 8.06% (V_{OC}: 0.95 V, J_{SC}: 11.27 mA/cm^2, and FF: 0.75), respectively. Interestingly, the $IC_{60}BA$-derived device showed the highest V_{OC} which can be rationalized from the fact that its LUMO is the highest among the three fullerenes. Consequently, the C_{60}-based HPSC should have the smallest V_{OC} of the three fullerenes because of C_{60}'s low LUMO. However, the C_{60}-based HPSC showed a comparable V_{OC} (0.92 V) to that of $PC_{61}BM$-based device (0.89 V). It can be envisaged that high C_{60} electron mobility effectively reduces charge recombination at the perovskite/C_{60} interface and diminishes potential loss across this interface. Besides, the hysteresis test of the studied devices was also performed. All the devices presented very minor hysteresis at a low scan rate of 0.01 V/s, suggesting limited charge traps at the perovskite interfaces (PEDOT:PSS/$MAPbI_3$ and $MAPbI_3$/fullerene). The improved J_{SC} and FF of $PC_{61}BM$- and C_{60}-based HPSCs can be interpreted as a consequence of improved charge dissociation/transport at the perovskite/fullerene interface arising from these fullerenes' increased electron mobility. The very minor hysteresis and high performance of HPSCs studied herein show that such charge redistribution at the perovskite/fullerene interface may also passivate interfacial trap states as well as reduce interfacial energy barrier. [94, 95] As a whole, this study more comprehensively elucidated the complex roles of fullerenes in enhancing the performance of HPSCs.[96]

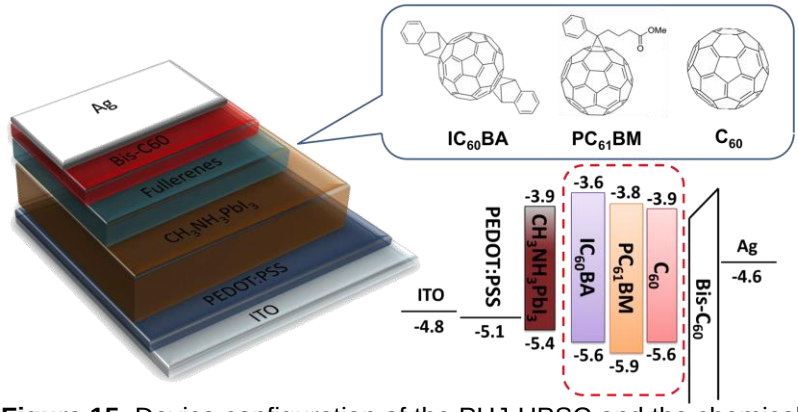

Figure 15. Device configuration of the PHJ HPSC and the chemical structures of the n-type fullerene derivatives, $IC_{60}BA$, $PC_{61}BM$ and C_{60} in this study. The energy diagram of the each layer in devices.

(c) TOPO surface Passivation leads to over 90% internal PLQY

Reducing non-radiative recombination in semiconducting materials is a prerequisite for achieving the highest performance in light-emitting and photovoltaic applications. Here, we characterize both external and internal photoluminescence quantum efficiency and quasi-Fermi-level splitting of surface-treated hybrid perovskite ($CH_3NH_3PbI_3$) thin films.

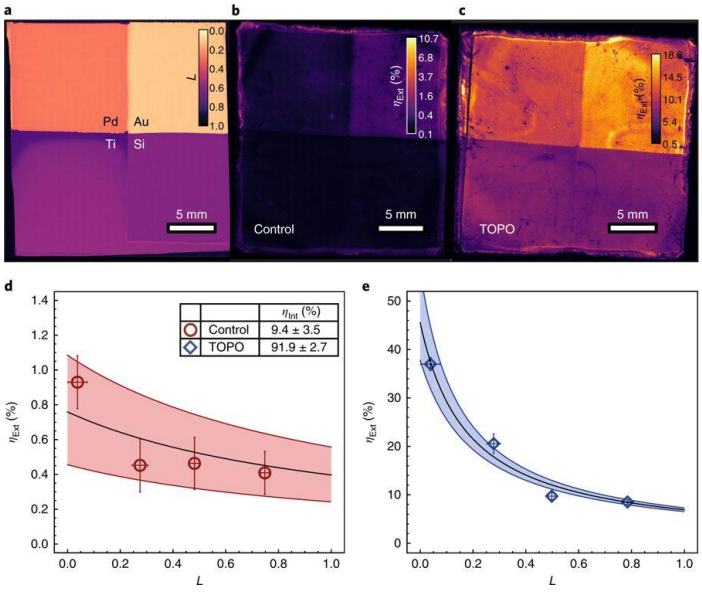

Figure 16. a spatial map showing measured optical loss factors, L = 1 − Reflectivity = 1 − R, of the Au, Pd, Ti and Si quadrants of the metal back-reflector substrate before perovskite deposition. b,c, Spatial map showing η_{ext} for a typical control (b) and TOPO-treated (c) film deposited on the multi-metal back-reflector substrate. d,e, η_{ext} data as a function of L for a control film and champion TOPO-treated film, respectively. Error bars, shaded areas and black lines are 95% confidence intervals over the spatial heterogeneity in the data points, 95% confidence intervals of the nonlinear regression, and nonlinear regression fits, respectively.

With respect to the material bandgap, these passivated films exhibit the highest quasi-Fermi-level splitting measured to date, reaching 97.1 ± 0.7% of the radiative limit, approaching that of the highest performing GaAs solar cells. We confirm these values with independent measurements of internal photoluminescence quantum efficiency of 91.9 ± 2.7% under 1 Sun illumination intensity, setting a new benchmark for these materials (Figure 16). These results suggest hybrid perovskite solar cells are inherently capable of further increases in power conversion efficiency if surface passivation can be combined with optimized charge carrier selective interfaces[97].

Subtask 4.2. Development of Single-Junction HP Solar Cells

(a) Stabilized Large Bandgap Perovskite Solar Cells by Tin Substitution

The current development of high efficiency wide bandgap (1.7−1.8 eV) HP solar cells utilizes controlled incorporation of Br into $MAPbI_3$ or $FAPbI_3$. The resultant compositionally engineered $MAPb(I_{1-y}Br_y)_3$ and $FAPb(I_{1-y}Br_y)_3$ perovskites possess tunable bandgaps of 1.57−2.29 eV and 1.48−2.23 eV, respectively. Despite many reported high efficiency devices, light-induced instability was commonly observed under the operating conditions (AM 1.5 illumination) for wide bandgap HP solar cells employing $MAPb(I_{1-y}Br_y)_3$ and $FAPb(I_{1-y}Br_y)_3$ perovskite compositions with Br content beyond 20% (y > 0.2).20 Under illumination, the complex phase segregation into iodide- and bromide-rich perovskite phases causes significant drop in photocurrent over time, which raises severe concerns for stable long-term operation of these solar cells.[98, 99] To develop an effective alternate

approach, we introduced Sn into the highly unstable $MAPb(I_{0.6}Br_{0.4})_3$ perovskite composition to form $MAPb_{1-x}Sn_x(I_{0.6}Br_{0.4})_3$. An optimum of 25% Sn substitution was identified based on the morphology and device performance. A combination of transient absorption spectroscopy (TAS) and X-ray diffractometry (XRD) analysis demonstrated elimination of phase segregation in $MAPb_{0.75}Sn_{0.25}(I_{0.6}Br_{0.4})_3$ and the existence of single stable phase under illumination. Introduction of Sn resulted in alteration of internal bonding environment (both crystallite size and lattice microstrain), which subsequently made the mixed halide perovskite less vulnerable to phase segregation during photostriction under illumination and thus improved photostability. The efficacy and versatility of this concept are further demonstrated by extending it to different Br contents in the $MAPb_{0.75}Sn_{0.25}(I_{1-y}Br_y)_3$ perovskite system (Figure 17). Finally, with the consideration for tandem solar cell application, a $MAPb_{0.75}Sn_{0.25}(I_{0.4}Br_{0.6})_3$ perovskite with a bandgap of 1.73 eV and stable PCE of 12.59% was demonstrated. Devices not only show constant photocurrent at maximum power point under 1 sun illumination (Figure 21d), but also can retain 95% of their original PCE after 30-day storage in inert atmosphere. They also possess respectable thermal stability at 85 °C under inert atmosphere.

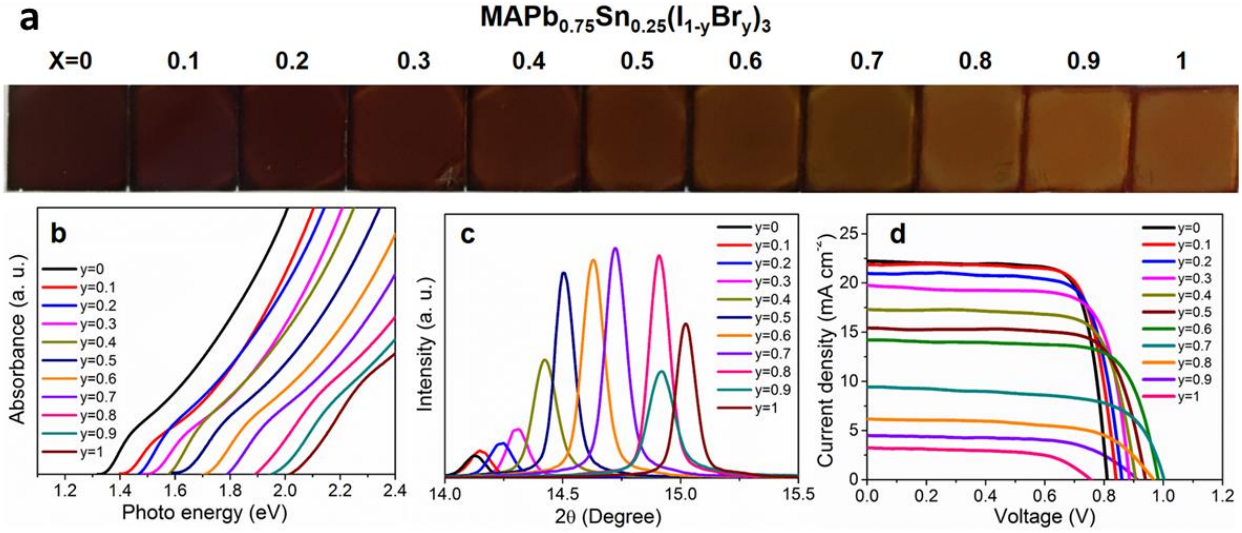

Figure 17. (a) Optical images, (b) absorption spectra, and (c) XRD spectra of $MAPb_{0.75}Sn_{0.25}(I_{1-y}Br_y)_3$ perovskites with different Br content. (d) Typical J−V characteristics of $MAPb_{0.75}Sn_{0.25}(I_{1-y}Br_y)_3$ PVSCs measured under AM 1.5 illumination.

(b) Stabilized Large Bandgap Perovskite Solar Cells by Cesium Substitution

Though we successfully eliminated photo-instability in $MAPb(I_{1-y}Br_y)_3$ alloys by partial Sn substitution as discussed above, the resultant $MAPb_{0.75}Sn_{0.25}(I_{1-y}Br_y)_3$ alloys suffer from low $V_{oc.}$ This is an indication of potentially poor optoelectronic quality of perovskite absorbers. We observe that even the best performing (12.59% PCE) composition $MAPb_{0.75}Sn_{0.25}(I_{0.6}Br_{0.4})_3$ show extremely low PLQY and longer iteration of signals (>30 min) or high intensity exposure (>100 Sun) under continuous illumination was inevitable to get discernible signals.[26] The poor emissivity is probably related to high material disorder in the 75% Pb - 25% Sn alloys due to phase transition from I4cm to P4mm, in accordance to previous reports.[100] This inherent limitation in material quality explains the severely constrained V_{oc} with partial Sn substitution. Therefore, as an alternate approach

to overcome photoinstability without compromising optoelectronic quality, we chose to engineer the lattice in an analogous manner, via partial replacement of MA by Cs. A series of single junction PVSCs were fabricated with 0-20% Cs substitution in $MAPb(I_{0.6}Br_{0.4})_3$ and we found that the device with 10% Cs showed the best device performance with high V_{oc} of 1.2 V, PCE of 12.5% and negligible J-V hysteresis (Figure 18a). $MA_{0.9}Cs_{0.1}Pb(I_{0.6}Br_{0.4})_3$ films were phase pure and exhibited relatively longer lifetime due to improved crystallinity with Cs incorporation.[101] As expected, striking differences were observed in photostability of $MAPb(I_{0.6}Br_{0.4})_3$ and $MA_{0.9}Cs_{0.1}Pb(I_{0.6}Br_{0.4})_3$-based PVSCs. With Cs incorporation, devices were photostable and current density at the maximum power point (MPP) was constant under continuous illumination (1 h), whereas devices without Cs showed significant decay in less than 10 min of illumination (Figure 18b). This stability under operating conditions is critical for 2-T tandem, where any change in subcell behavior will impact current matching and significantly degrade tandem performance. Optoelectronic quality and photovoltage losses were evaluated for $MA_{0.9}Cs_{0.1}Pb(I_{0.6}Br_{0.4})_3$ using time-resolved photoluminescence (TRPL) spectroscopy. Absolute PL intensity spectra and absorbance are shown in the inset of Figure 18c and the E_g is 1.82 eV. A relatively stable QFLS ≈1.23 eV was observed which correlates well with the device V_{oc} (Figure 23c). To enable monolithic tandem with CIS bottom cell, the top Ag electrode was replaced with sputtered ITO which transmits unabsorbed light efficiently. The resultant devices performed well and showed a V_{oc} of 1.22 V, a J_{sc} of 12.1 mA cm^{-2}, a FF of 0.69 and a PCE of 10.1% (Figure 18a), analogous to Ag electrode devices discussed above. The drop in J_{sc} is reasonable considering an increased transmittance of long wavelength light through top ITO. The device stack is unaffected during sputtering and the superior performance of semitransparent devices without compromise in V_{oc} ensures high optoelectronic quality of sputtered ITO.

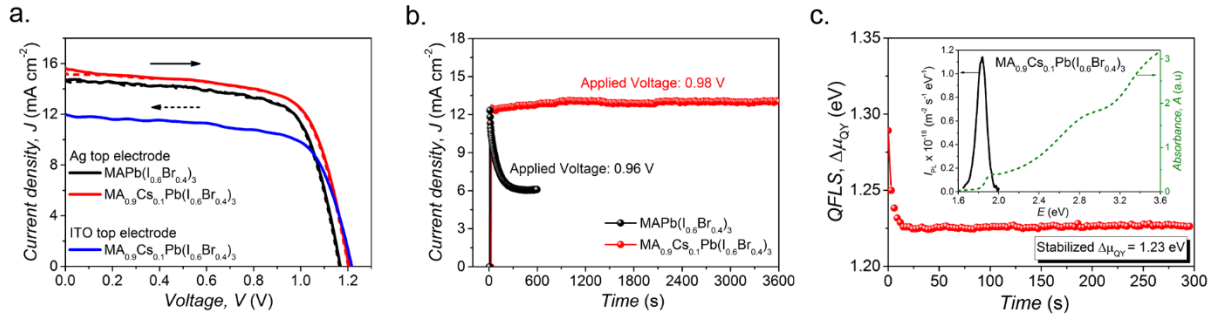

Figure 18. (a) Typical J–V characteristics and (b) steady-state current under AM1.5 illumination at an applied voltage corresponding to MPP of $MAPb(I_{0.6}Br_{0.4})_3$ and $MA_{0.9}Cs_{0.1}Pb(I_{0.6}Br_{0.4})_3$ PVSCs. (c) Stabilized quasi-Fermi level splitting of $MA_{0.9}Cs_{0.1}Pb(I_{0.6}Br_{0.4})_3$ with initial PL spectra and absorbance shown in figure inset.

(c) PEA-Incorporated Large E_g Perovskites with Improved Optoelectronic Quality

Here, we demonstrate the effectiveness of phenylethylammonium (PEA) incorporation for solving the inherent material challenges and minimizing the $V_{oc,loss}$ in 1.8 eV E_g mixed-halide hybrid PVSCs. We systematically tuned the composition by mixing $MAPb(I_{0.6}Br_{0.4})_3$ and $(PEA)_2Pb(I_{0.6}Br_{0.4})_4$ precursor solutions in different ratios to get the desired PEA fraction (**Figure 19a, b**). As PEA fraction increases from PEA0 to PEA20, E_g increases subtly from 1.82 to 1.84 eV. With further increase in PEA fraction, E_g increases more significantly and reaches 2.56 eV (PEA100) (**Figure 19b**). From XRD studies, it is evident

that the fwhm increases due to continuous decrease in crystallite size from 112 ± 9nm (PEA0) to 23 ± 1 nm (PEA20), and the contribution from strain is almost constant for PEA0-PEA20 (**Figure 19c**). The decrease in crystallite size can be attributed to the impeded growth by PEA-induced surface functionalization of perovskite crystallites, where the large ammonium cations cannot be incorporated into the 3D lattice and act as surface capping ligands[102]. Therefore, as the PEA fraction is increased, a decrease in the crystallite size of 3D perovskite coupled with an increase in the formation of layered perovskites are expected. PEA incorporation in $MAPb(I_{0.6}Br_{0.4})_3$ led to enhancements in photostability as well as optoelectronic quality and improved the QFLS up to 1.35 eV (**Figure 19d**). Based on insights from detailed structural and spectroscopic studies, we infer that a combination of the decrease in crystallite size and L_d along with the modification of grain boundaries by PEA ligands (anchoring on perovskite surfaces) contribute to mitigation of phase segregation in PEA5−PEA20. Our results provide an important validation for the emerging mechanistic picture and the current understanding of phase segregation in mixed-halide perovskites. Subsequently with interface optimization, PVSCs based on PEA-incorporated 1.80−1.85 eV E_g absorbers yielded significantly improved V_{oc} values of 1.30−1.35 V and were stable under illumination (**Figure 19d, e**). The achieved Voc/Voc,SQ values of 0.85−0.87 surpass the photo-voltage plateau in 1.8 eV Eg PVKSCs. This work has been published in *Nano Letters*[103].

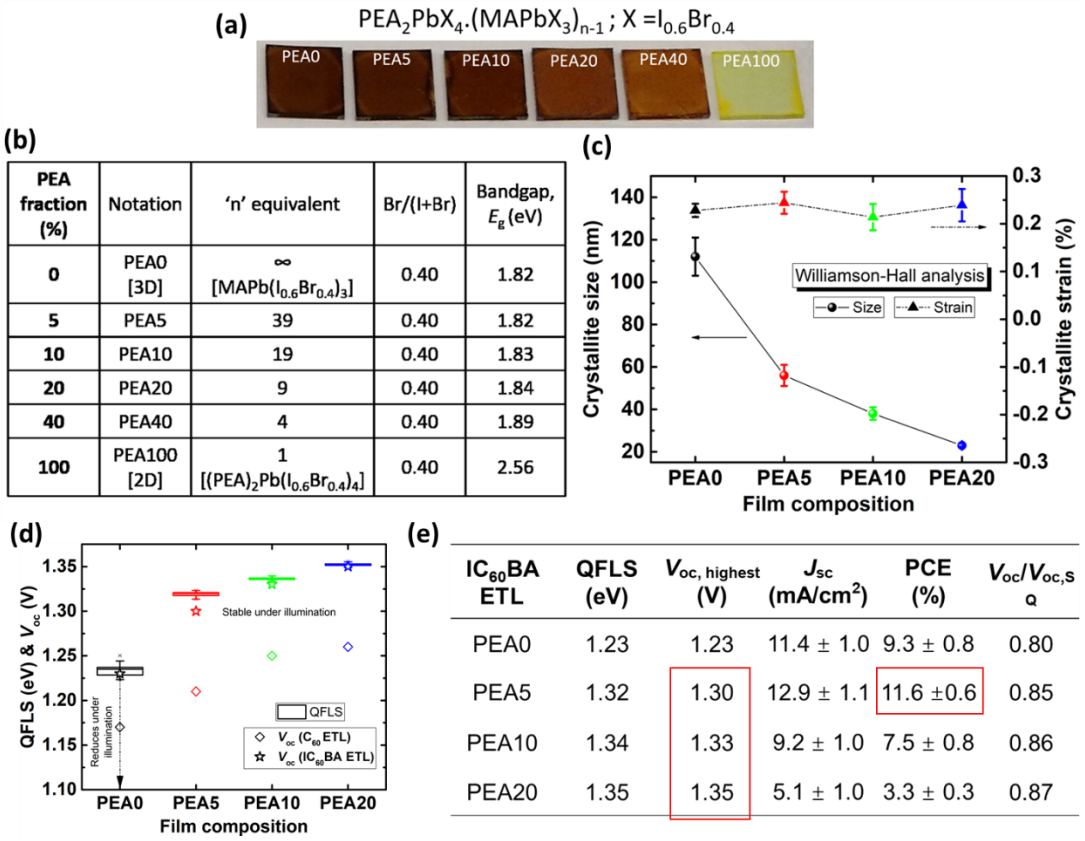

PEA fraction (%)	Notation	'n' equivalent	Br/(I+Br)	Bandgap, E_g (eV)
0	PEA0 [3D]	∞ $[MAPb(I_{0.6}Br_{0.4})_3]$	0.40	1.82
5	PEA5	39	0.40	1.82
10	PEA10	19	0.40	1.83
20	PEA20	9	0.40	1.84
40	PEA40	4	0.40	1.89
100	PEA100 [2D]	1 $[(PEA)_2Pb(I_{0.6}Br_{0.4})_4]$	0.40	2.56

$IC_{60}BA$ ETL	QFLS (eV)	$V_{oc,\ highest}$ (V)	J_{sc} (mA/cm^2)	PCE (%)	$V_{oc}/V_{oc,SQ}$
PEA0	1.23	1.23	11.4 ± 1.0	9.3 ± 0.8	0.80
PEA5	1.32	1.30	12.9 ± 1.1	11.6 ±0.6	0.85
PEA10	1.34	1.33	9.2 ± 1.0	7.5 ± 0.8	0.86
PEA20	1.35	1.35	5.1 ± 1.0	3.3 ± 0.3	0.87

Figure 19. (a) Photographs of films with 0 to 100% PEA fraction ([moles of PEA]/[moles of PEA + moles of MA]) in $MAPb(I_{0.6}Br_{0.4})_3$ perovskite. (b) Definition of notations used to represent different compositions and their associated E_g values. n equivalent corresponds to the number of metal-halide sheets sandwiched between PEA cations if a pure 2D perovskite can be formed; 5− 40% PEA fractions here form quasi-2D perovskite, which is a mixture of 3D and 2D perovskite phases with different n values. (c) Crystallite size

and strain values obtained using Williamson-Hall analysis of peak broadening in powder samples. (d) Comparison of quasi-Fermi level splitting (QFLS) and V_{oc} values for PEA0-PEA20 devices with C_{60} and $IC_{60}BA$ ETL. (e) PV performance metrics of PEA0-PEA20 devices with $IC_{60}BA$ ETL.

(d) GA-alloying and interface engineering enables High V_{oc}

The above work demonstrates improved bulk perovskite optoelectronic quality for both the $MAPb(I,Br)_3$ + PEAI and the $(FA,GA,Cs)Pb(I,Br)_3$ system. In addition, the $MAPb(I,Br)_3$ + PEAI system demonstrates incredible interface quality – the ΔE_F of the neat HP film is quite close to both the ΔE_F of HP film in contact with transport layers and the V_{OC}. However, one disadvantage of the 2D/3D system is reduction in L_D and J_{SC}. On the other hand, the the $(FA,GA,Cs)Pb(I,Br)_3$ system gives provides higher L_D and adequate carrier transport, but the interface quality is slightly lower (ΔE_F is higher than attained V_{OC})[21]. Interface recombination was reduced by replacing C_{60} with ICBA (see Figure 20), yet V_{OC}s are still below the ΔE_F of neat HP film. Thus, we fabricated a bilayer system, with $(FA,GA,Cs)Pb(I,Br)_3$ bulk, then post treatment with PEAI to form a thin 2D/3D layer on the top surface. This strategy has shown promise in achieving excellent interface quality without significant loss in L_D. With this strategy, we have achieved V_{OC}s of 1.29V for a 1.75eV HP (88% of the Shockley-Queisser limit, see Figure 20. We are presently studying this system further to realize its full potential and also reveal stability benefits of this bilayer HP structure.

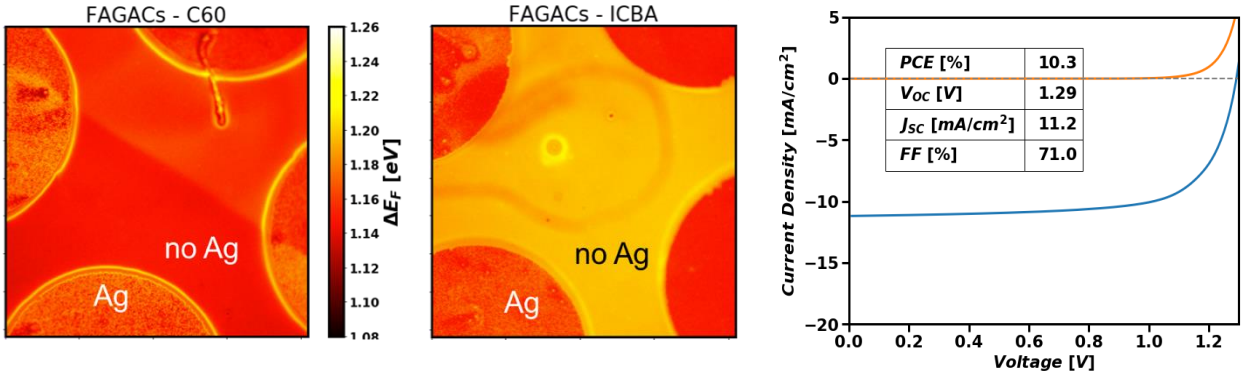

Figure 20. ΔE_F determined by wide-field PL imaging for completed FAGACs devices, with C_{60} as electron transport layer (ETL) (left) and with ICBA and ETL (center). The brighter PL and higher ΔE_F for ICBA case indicates that there is less interface recombination, allowing for higher V_{OC}. High V_{OC} of 1.29V, or 88% of SQ limit is demonstrated for 1.75eV GA-based HP solar cell with PEAI interface engineering (right).

(e) Summary of Advances in High Bandgap Photovoltage Compared to Literature

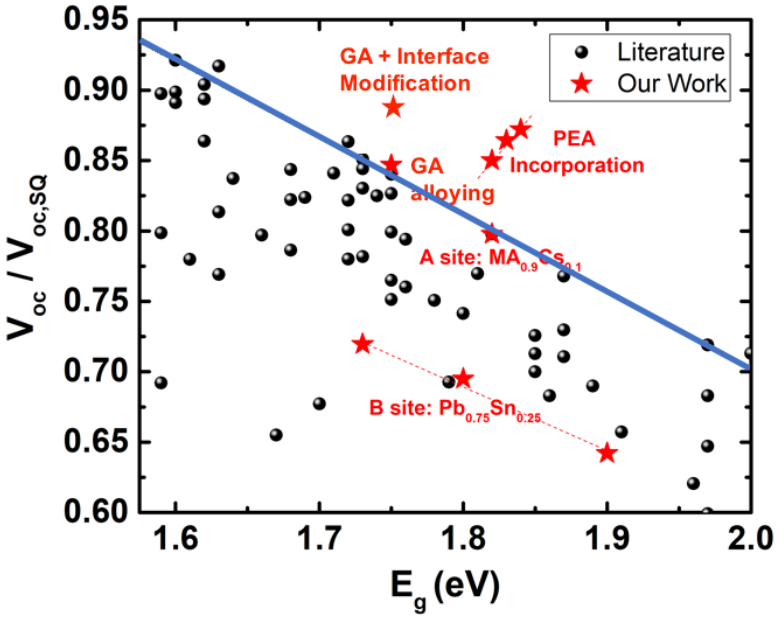

Figure 21. V_{OC} presented as a fraction of the SQ limit appears to decrease with increasing bandgap. Advance in photovoltage from our work are shown as stars, compared to other results in literature.

Task 5: Developing Interconnect Layers

The interconnect layer for a tandem solar cell must have low series resistance at the operating point and high transparency in the NIR to allow efficient operation of the bottom cell. We tested three HTMs to determine their suitability in this regard: spiro-MeOTAD, PEDOT:PSS, and copper-doped nickel oxide (Cu:NiO_x), all prepared on ITO (which is the top electron extracting contact for the CIGS bottom cell). Figure 14 shows the location of the interconnect layer in a tandem device and the architectures used for interconnect testing. We also considered the effect of annealing temperature on the properties of these HTMs as the device stack will need to be annealed after deposition of the interconnect layer. JV testing (Figure 22) showed all three to be Ohmic. By taking the slope (m) of the positive bias region, we can determine the series resistance. Table 1 gives the extracted values for R_S in both Ω*cm^2 and Ω. All of the HTMs tested showed series resistances well below our targeted of 9.3 Ω*cm^2. The Cu:NiOx has the lowest series and sheet resistance, therefore this is the HTM we further characterized with UV-Vis spectroscopy. The shaded and bounded region in Figure 23 shows our target of >70 %T between 750 and 1150 nm. Once again, all the HTMs beat the 70 %T goal, with the low-temperature annealed Cu:NiO_x being the best.

	R_S (Ω*cm^2)	R_S (Ω)	R (Ω/square)
Cu:NiOx at 150°C	0.497	9.95	19.6
Cu:NiOx at 200°C	0.547	10.9	22.
Cu:NiOx at 225°C	0.59	11.8	21.9
PEDOT:PSS	0.769	15.4	–
spiro–MeOTAD	1.	20.	–

Table 1: Series and sheet resistance of the HTMs

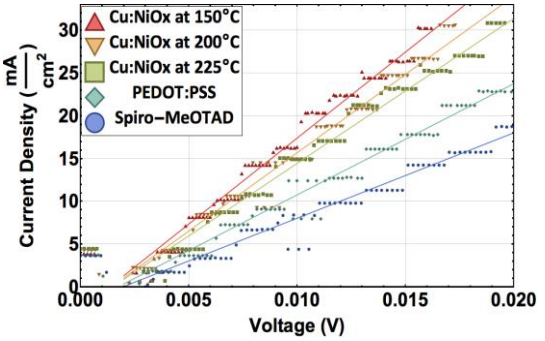

Figure 22. JV testing of Cu:NiOx annealed at different temperatures, PEDOT:PSS and spiro-MeOTAD

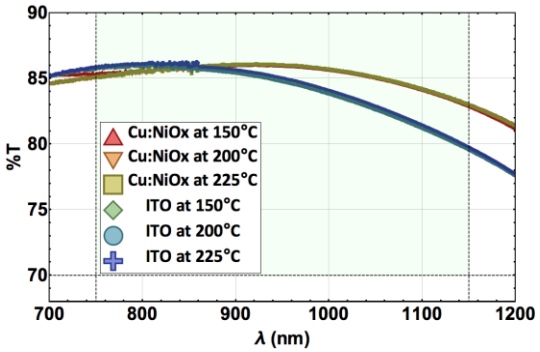

Figure 23. Transmittance spectra of bare ITO and Cu:NiO_x/ITO annealed at different temperatures

In conclusion, we have tested three different interconnects, meeting *Milestone 5.1.* Additionally, all of our fabricated interconnects have J > 18 mA/cm^2, R_S < 9.3 Ω*cm^2, and %T > 70 between 750 and 1150 nm, meaning ***we have met and exceeded Milestone 5.2 which is also Go/No-Go 4.*** The low-temperature annealed Cu:NiOx/ITO is the best on all metrics, and will be a focus of ongoing work.

Task 6: Development of Tandem Hybrid Perovskite / Chalcogenide Solar Cells

(a) Mechanically stacked Perovskite – CIGS tandem results

Solution-processed chalcopyrite and perovskite devices of various bandgaps are combined in four- and two-terminal mechanically-stacked tandem architectures. The excellent low-light performance of Cu(In,Ga)(S,Se)$_2$ and low-bandgap CuIn(S,Se)$_2$ cells and the high efficiency of novel NIR-transparent inverted perovskite cells with C_{60}/bis-C_{60}/ITO as electron transport layers, enabled stabilized two- and four-terminal tandem efficiencies up to 18.5% and 18.8%, respectively, which represent a new record for tandem devices with solution-processed chalcopyrite and perovskite absorbers[104] (Figure 24).

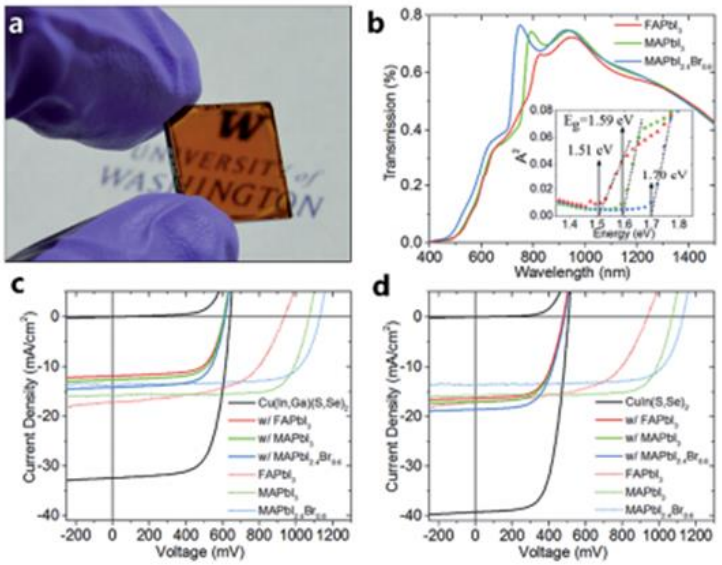

Figure 24. (a) Photograph of a semi-transparent perovskite solar cell. (b) Transmission and squared absorbance of perovskite filters used in Table 1. The bandgaps are extracted to 1.51 eV, 1.59 eV, and 1.70 eV for $FAPbI_3$, $MAPbI_3$, and $MAPbI_{2.4}Br_{0.6}$, respectively. (c and d) *J*(*V*) measurements of perovskite cells, CI(G)S devices, and CI(G)S devices with perovskite filters. (e and f) External quantum efficiency data of perovskites and shaded chalcogenide cells that yielded the highest two-terminal tandem PCEs in this paper (projected PCE). Excellent current matching is obtained for Cu(In,Ga)(S,Se)$_2$ and $MAPbI_{2.4}Br_{0.6}$ as well as for CuIn(S,Se)$_2$ and $MAPbI_3$, and CuIn(S,Se)$_2$ and $FAPbI_3$, respectively.

(b) Monolithic HP – CIGS tandems

To demonstrate the suitability of our solution-processed low-bandgap CIS devices as bottom cells in tandem applications, we fabricated monolithic tandem devices with solution-processed perovskite top cells. Similar to previously described, perovskite devices were manufactured in an inverted ITO/HTL/$MAPbI_3$/C_{60}/bis-C_{60}/cathode architecture with poly(3,4-ethylenedioxythiophene) polystyrene sulfonate (PEDOT:PSS) or NiO_x as hole transport layer (HTL)[18]. While we could effectively reduce the absorber roughness of our CIS bottom devices by employing a Cu-graded precursor approach (see Figure 25b), the increased roughness as compared to glass (2–5 nm) is still a challenge for the PSC due to the inherent thin film nature of the involved functional layers. To further reduce the likelihood of shunt paths in the PSC top cell via accidental anode and cathode contact, the perovskite absorber thickness was increased from 180–220 to 550–600 nm and the C_{60} electron transport layer (ETL) was thermally evaporated rather than spin-coated to ensure conformal coverage. Current–voltage characterization under ambient air conditions revealed a strong light-soaking behavior for tandems with both HTLs. Figure 25c shows the improving device parameters during maximum power point (MPP) tracking under simulated AM1.5G light for a PEDOT:PSS-based tandem device. Device performance was seen to stabilize at up to 8.55% after 4.5 h. A comparison of the initial and stabilized *J*–*V* curve reveals key improvements through increasing FF with MPP tracking (FF_0 = 18.4%, FF_{stab} = 42.1%, see Figure 3d). Stabilized tandem V_{oc}'s of up to 1.40 V are close to the added voltages of the individual cells (i.e., CIS: 518 mV, PSC(PEDOT:PSS): 975 mV, sum: 1.49 V) which suggests a good monolithic contact between top and bottom cells and low leakage currents. Notably, we were able to relate the source for our poor FF to our semitransparent perovskite top cells. Poor morphologies of HP layers, as seen in Figure 25b, that are likely caused by use of rough CIS substrates might further exacerbate this issue. Further improvements in carrier diffusion lengths in the HP via defect passivation or morphology improvements or the use of thinner HP absorbers might remedy this problem and further increase tandem PCEs.

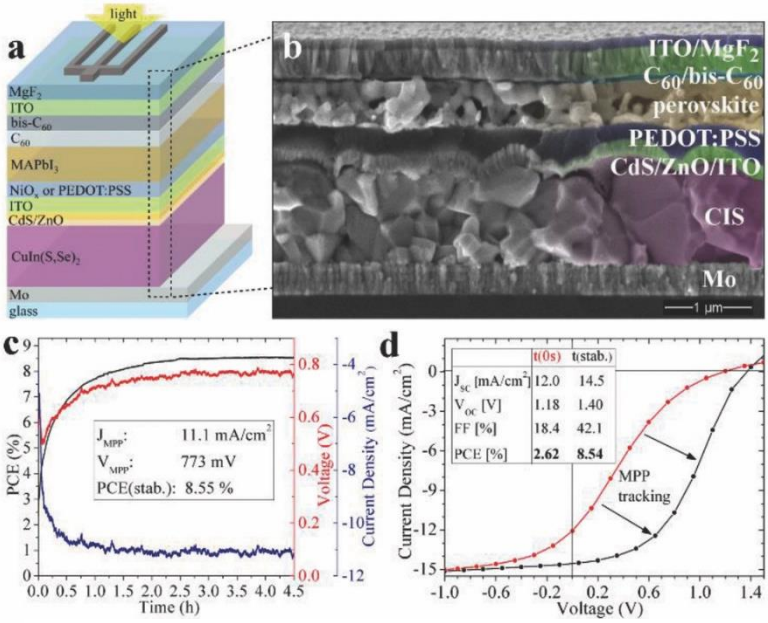

Figure 25. a) Schematic of monolithic HP-CIS tandem solar cell. b) SEM cross section of tandem solar cell. c,d) Maximum power point tracking shows improving and stabilizing active area PCE from initial 2.6% up to 8.6% after 4 h.

(c) 2-terminal monolithic HP – HP tandems

We also integrated our developed small and large bandgap subcells to fabricate 2-terminal monolithic perovskite-perovskite tandem solar cells. Figure 5a shows the cross-section scanning electron microscopy (SEM) image of a typical tandem cell where clear demarcation between layers are observed. J–V characteristics of the best performing 2-T tandem (Figure 26b) shows an exceptional V_{oc} of 1.98 V, a J_{sc} of 12.7 mA cm−2, and a FF of 0.73 resulting in a remarkable PCE of 18.4%. The EQE of subcells (Figure 26c) showed excellent current matching as predicted by optical simulations and integrated currents agree well with the J_{sc} obtained from J–V characteristics. The reliability of PCE was further confirmed by measuring the steady-state current output at MPP (1.55 V) which provided a stabilized efficiency of 18.5%. An absolute PCE improvement of ≈4% is realized compared to single-junction device (Figure 5b). A large V_{oc} (1.98 V) close to the sum of subcell V_{oc}'s realized for tandem cell manifests the effectiveness of rational design in our work. This is a significant improvement com- pared to previously reported V_{oc} (1.66 V) for similar bandgap- matched 2-T perovskite tandem[48]. To provide broader outlook, the 2-T perovskite tandem developed here was also compared with other state-of-the-art series connected tandem cells (Figure 5d), where PVSC is seamlessly coupled with another PV technology (organic photovoltaic (OPV), copper indium gallium selenide (CIGS), and Silicon). The 2-T perovskite tandem developed here has a nonideal loss fraction (≈17%) lower than the record silicon-perovskite tandem and the realized Voc (1.98 V) corresponds to an impressive ≈80% of the theoretical limit (Figure 26d).

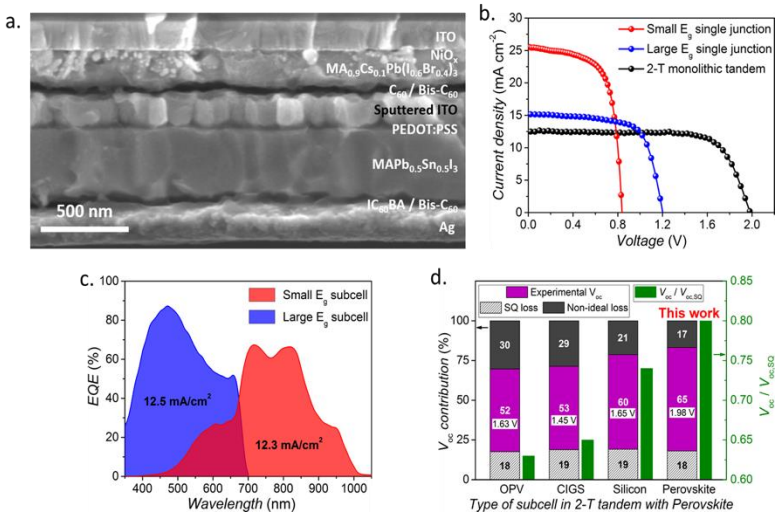

Figure 26. a) Cross-section SEM of a characteristic monolithic tandem device. b) Typical J–V characteristics of 2-terminal tandem solar cell along with that of the small- and large-bandgap single-junction solar cells with Ag electrode. c) EQE spectra of individual subcells in 2-terminal monolithic tandem. d) Fractional contribution of V_{oc} and associated losses with respect to bandgap for different state-of-art tandem solar cells, where perovskite is monolithically integrated with other photovoltaic technologies.

Conclusions:

The project successfully achieved all go/no-go metrics and fully met 27 of the 34 milestones. The remaining 7 milestones were achieved partially. In the process of achieving these milestones, the project revealed deeper understanding of the optoelectronic quality, morphology and phase control, interface passivation, and device fabrication of hybrid perovskites. Some of the key achievements were:

- Development of higher-performance high-bandgap (1.75 eV) perovskite materials and devices. In particular, we explored tens-of-thousands of compositions for high bandgap perovskites, achieving quasi-Fermi level splitting of 1.35 eV for a 1.75 eV bandgap material. We achieved World-record open circuit voltages from single junction p-i-n devices, 1.24 V from 1.75 eV bandgap material, which is what is preferable for tandems with a PCE of 14.3% using a guanidinium/formanadinium/ cesium alloyed lead iodobromide. We also developed a series of World-record efficiency devices at higher band-gaps based on 2D/3D perovskites using PEA.
- Development of higher-performance low-bandgap (1.35 eV) perovskite materials and devices. In particular, we developed a 1.35 eV bandgap perovskite of composition $MAPb_{0.5}Sn_{0.5}(I_{0.8}Br_{0.2})_3$ and showed its superiority to $MAPb_{0.75}Sn_{0.25}I_3$. High efficiency solar cells were fabricated using PEDOT:PSS and doped-ICBA as HTL and ETL, respectively. Short circuit currents of 25.7 mA/cm^2 and PCEs of 17.1% were obtained.
- Development of mechanically stacked 4-terminal CIGS-Perovskite tandems with PCE of 18.8% and monolithic 2-terminal CIGS-Perovskite tandems with PCE of 8.5%. The low efficiency of the monolithic device is a result of the high surface roughness of the solution processed CIGS bottom cells. This is not an intrinsic problem for CIGS-perovskite tandems, but does mean that smooth evaporated or sputtered CIGS films likely need to be used, unless a polishing step is employed.
- Development of monolithic 2-terminal Perovskite-Perovskite tandems with a stabilized PCE of 18.5%. This was the World-record perovskite-perovskite monolithic tandems for over a year in 2017-2018.
- Revealing that light is not an essential component of the so-called “light-induced” phase segregation. By using charge injection in the dark and electroluminescence, we showed that the presence of electrons in the conduction band and hole in the valence band is sufficient to drive the nearly ubiquitously observed phase segregation in high bandgap perovskites.
- Development of a new method to simultaneously measure absolute intensity photoluminescence and photoconductivity and use them to obtain simultaneous in-situ measurement of quasi-Fermi level splitting and diffusion length. This is important since it provides a proxy for device Voc and device Jsc.

Budget and Schedule:

The federal share of the budget was $1.5M. The University of Washington contributed a cost share of $167k. Both the federal share and cost share were fully spent with no deviations from the spend plan.

Path Forward:

The perovskite-silicon tandem record has now reached a certified efficiency of 27.3% (OxfordPV), which exceeds the record for a single junction silicon solar cell. This success shows the increasing potential benefit of using perovskites in multi-junction devices, whether with Si, CIGS, or in a perovskite-perovskite tandem configuration. We believe the most important topics to pursue in order to insure that such tandems have a significant impact on the energy future are:

1. Assessment and improvement of long term stability of perovskite devices when subject to environmental stresses of oxygen and humidity and operational stresses of electric fields and excess (non-equilibrium) electron and hole populations.
2. Deeper understanding of factors limiting the device performance for high bandgap (1.75-1.85eV) and low bandgap (1.20-1.30eV) HPs
3. Advances in interface engineering to realize further improvement in device efficiencies.
4. Employing lower dimensional perovskites to further enhance perovskite stability.

The work conducted under this award provides a strong foundation to enable continued advances in each of these thrusts. In particular, perovskite-perovskite tandems may have significant impact on the future of solar energy conversion to electricity. Although the highest efficiency perovskite-perovskite tandem that we have reported had a PCE of 18.5%, we have significantly improved our top and bottoms cell technology since focusing on perovskite-perovskite tandems. Combination of our best perovskite top and bottom cell would yield 2-terminal efficiency of about 24%. This would be a substantial improvement and set a new World-record. Whether by us or others, we believe that the high bandgap GA/FA/Cs perovskites and the PEA-based 2D/3D perovskites that we have developed along with the low bandgap Pb-Sn devices we have developed should be developed further an integrated into a fully optimized tandem.

However, the most significant challenge for perovskites is stability. If devices cannot survive 20-30 years with year-over-year degradation rates of ~1%, then they will have limited impact on the energy sector. Thus, we believe that it is imperative that additional research be devoted to this topic. Standardized accelerated aging tests need to be developed that probe the stability of the material to the simultaneous presence of oxygen humidity, and light, and the cycling through light/dark periods. New methods developed under this award, specifically the photoluminescence-photoconductivity method to simultaneously determine QFLS and diffusion length, provide a way to rapidly assess material stability and isolate interface problems.

Publications Resulting from This Work:

(1) Zhu, Z.; Bai, Y.; Liu, X.; Chueh, C.-C.; Yang, S.; Jen, A. K.-Y. Enhanced Efficiency and Stability of Inverted Perovskite Solar Cells Using Highly Crystalline SnO 2 Nanocrystals as the Robust Electron-Transporting Layer. *Adv. Mater.* **2016**, *28* (30), 6478–6484.

(2) Chen, J.-Y.; Chueh, C.-C.; Zhu, Z.; Chen, W.-C.; Jen, A. K.-Y. Low-Temperature Electrodeposited Crystalline SnO2 as an Efficient Electron-Transporting Layer for Conventional Perovskite Solar Cells. *Sol. Energy Mater. Sol. Cells* **2017**, *164* (February), 47–55.

(3) Zhao, T.; Williams, S. T.; Chueh, C.-C.; DeQuilettes, D. W.; Liang, P.-W.; Ginger, D. S.; Jen, A. K.-Y. Design Rules for the Broad Application of Fast (<1 s) Methylamine Vapor Based, Hybrid Perovskite Post Deposition Treatments. *RSC Adv.* **2016**, *6* (33), 27475–27484.

(4) Xu, X.; Chueh, C.-C.; Yang, Z.; Rajagopal, A.; Xu, J.; Jo, S. B.; Jen, A. K.-Y. Ascorbic Acid as an Effective Antioxidant Additive to Enhance the Efficiency and Stability of Pb/Sn-Based Binary Perovskite Solar Cells. *Nano Energy* **2017**, *34*, 392–398.

(5) Stoddard, R. J.; Rajagopal, A.; Palmer, R. L.; Braly, I. L.; Jen, A. K.-Y.; Hillhouse, H. W. Enhancing Defect Tolerance and Phase Stability of High-Bandgap Perovskites via Guanidinium Alloying. *ACS Energy Lett.* **2018**, *3* (6), 1261–1268.

(6) Yang, Z.; Chueh, C.-C.; Liang, P.-W.; Crump, M.; Lin, F.; Zhu, Z.; Jen, A. K.-Y. Effects of Formamidinium and Bromide Ion Substitution in Methylammonium Lead Triiodide toward High-Performance Perovskite Solar Cells. *Nano Energy* **2016**, *22*, 328–337.

(7) Xu, X.; Chueh, C.-C.; Jing, P.; Yang, Z.; Shi, X.; Zhao, T.; Lin, L. Y.; Jen, A. K.-Y. High-Performance Near-IR Photodetector Using Low-Bandgap MA 0.5 FA 0.5 Pb 0.5 Sn 0.5 I 3 Perovskite. *Adv. Funct. Mater.* **2017**, *27* (28), 1701053.

(8) Yang, Z.; Chueh, C.-C.; Zuo, F.; Kim, J. H.; Liang, P.-W.; Jen, A. K.-Y. High-Performance Fully Printable Perovskite Solar Cells via Blade-Coating Technique under the Ambient Condition. *Adv. Energy Mater.* **2015**, *5* (13), 1500328.

(9) Braly, I. L.; Stoddard, R. J.; Rajagopal, A.; Jen, A. K.-Y.; Hillhouse, H. W. Photoluminescence and Photoconductivity to Assess Maximum Open-Circuit Voltage and Carrier Transport in Hybrid Perovskites and Other Photovoltaic Materials. *J. Phys. Chem. Lett.* **2018**, *9* (13), 3779–3792.

(10) Zhu, Z.; Zhao, D.; Chueh, C.-C.; Shi, X.; Li, Z.; Jen, A. K.-Y. Highly Efficient and Stable Perovskite Solar Cells Enabled by All-Crosslinked Charge-Transporting Layers. *Joule* **2018**, *2* (1), 168–183.

(11) Rajagopal, A.; Yao, K.; Jen, A. K.-Y. Toward Perovskite Solar Cell Commercialization: A Perspective and Research Roadmap Based on Interfacial Engineering. *Adv. Mater.* **2018**, *30* (32), 1800455.

(12) Li, N.; Zhu, Z.; Li, J.; Jen, A. K.-Y.; Wang, L. Inorganic CsPb 1− x Sn x IBr 2 for Efficient Wide-Bandgap Perovskite Solar Cells. *Adv. Energy Mater.* **2018**, *8* (22), 1800525.

(13) Braly, I. L.; Stoddard, R. J.; Rajagopal, A.; Uhl, A. R.; Katahara, J. K.; Jen, A. K.; Hillhouse, H. W. Current-Induced Phase Segregation in Mixed Halide Hybrid Perovskites and Its Impact on Two-Terminal Tandem Solar Cell Design. *ACS Energy Lett.* **2017**, *2* (8), 1841–1847.

(14) Rajagopal, A.; Stoddard, R. J.; Jo, S. B.; Hillhouse, H. W.; Jen, A. K.-Y. Overcoming the Photovoltage Plateau in Large Bandgap Perovskite Photovoltaics. *Nano Lett.* **2018**, *18* (6), 3985–3993.
(15) Kim, J. H.; Chueh, C.-C.; Williams, S. T.; Jen, A. K.-Y. Room-Temperature, Solution-Processable Organic Electron Extraction Layer for High-Performance Planar Heterojunction Perovskite Solar Cells. *Nanoscale* **2015**, *7* (41), 17343–17349.
(16) Williams, S. T.; Rajagopal, A.; Chueh, C.-C.; Jen, A. K.-Y. Current Challenges and Prospective Research for Upscaling Hybrid Perovskite Photovoltaics. *J. Phys. Chem. Lett.* **2016**, *7* (5), 811–819.
(17) Jung, J. W.; Williams, S. T.; Jen, A. K.-Y. Low-Temperature Processed High-Performance Flexible Perovskite Solar Cells via Rationally Optimized Solvent Washing Treatments. *RSC Adv.* **2014**, *4* (108), 62971–62977.
(18) Yang, Z.; Rajagopal, A.; Jo, S. B.; Chueh, C.-C.; Williams, S.; Huang, C.-C.; Katahara, J. K.; Hillhouse, H. W.; Jen, A. K.-Y. Stabilized Wide Bandgap Perovskite Solar Cells by Tin Substitution. *Nano Lett.* **2016**, *16* (12), 7739–7747.
(19) Jung, J. W.; Chueh, C.-C.; Jen, A. K.-Y. High-Performance Semitransparent Perovskite Solar Cells with 10% Power Conversion Efficiency and 25% Average Visible Transmittance Based on Transparent CuSCN as the Hole-Transporting Material. *Adv. Energy Mater.* **2015**, *5* (17), 1500486.
(20) Ju, D.; Dang, Y.; Zhu, Z.; Liu, H.; Chueh, C.-C.; Li, X.; Wang, L.; Hu, X.; Jen, A. K.-Y.; Tao, X. Tunable Band Gap and Long Carrier Recombination Lifetime of Stable Mixed CH 3 NH 3 Pb x Sn 1– x Br 3 Single Crystals. *Chem. Mater.* **2018**, *30* (5), 1556–1565.
(21) Liu, X.; Chueh, C.-C.; Zhu, Z.; Jo, S. B.; Sun, Y.; Jen, A. K.-Y. Highly Crystalline Zn 2 SnO 4 Nanoparticles as Efficient Electron-Transporting Layers toward Stable Inverted and Flexible Conventional Perovskite Solar Cells. *J. Mater. Chem. A* **2016**, *4* (40), 15294–15301.
(22) Li, Z.; Zhu, Z.; Chueh, C.; Luo, J.; Jen, A. K. -Y. Facile Thiol-Ene Thermal Crosslinking Reaction Facilitated Hole-Transporting Layer for Highly Efficient and Stable Perovskite Solar Cells. *Adv. Energy Mater.* **2016**, *6* (21), 1601165.
(23) Rajagopal, A.; Williams, S. T.; Chueh, C.-C.; Jen, A. K.-Y. Abnormal Current–Voltage Hysteresis Induced by Reverse Bias in Organic–Inorganic Hybrid Perovskite Photovoltaics. *J. Phys. Chem. Lett.* **2016**, *7* (6), 995–1003.
(24) Li, C.-Z.; Liang, P.-W.; Sulas, D. B.; Nguyen, P. D.; Li, X.; Ginger, D. S.; Schlenker, C. W.; Jen, A. K.-Y. Modulation of Hybrid Organic–perovskite Photovoltaic Performance by Controlling the Excited Dynamics of Fullerenes. *Mater. Horiz.* **2015**, *2* (4), 414–419.
(25) Wang, Q.; Chueh, C.-C.; Eslamian, M.; Jen, A. K.-Y. Modulation of PEDOT:PSS PH for Efficient Inverted Perovskite Solar Cells with Reduced Potential Loss and Enhanced Stability. *ACS Appl. Mater. Interfaces* **2016**, *8* (46), 32068–32076.
(26) Rajagopal, A.; Liang, P.-W.; Chueh, C.-C.; Yang, Z.; Jen, A. K.-Y. Defect Passivation via a Graded Fullerene Heterojunction in Low-Bandgap Pb–Sn Binary Perovskite Photovoltaics. *ACS Energy Lett.* **2017**, *2* (11), 2531–2539.
(27) Kim, J. H.; Liang, P.; Williams, S. T.; Cho, N.; Chueh, C.; Glaz, M. S.; Ginger, D. S.; Jen, A. K.-Y. High-Performance and Environmentally Stable Planar Heterojunction Perovskite Solar Cells Based on a Solution-Processed Copper-Doped Nickel Oxide Hole-Transporting Layer. *Adv. Mater.* **2015**, *27* (4), 695–701.

(28) Liu, X.; Yang, Z.; Chueh, C.-C.; Rajagopal, A.; Williams, S. T.; Sun, Y.; Jen, A. K.-Y. Improved Efficiency and Stability of Pb–Sn Binary Perovskite Solar Cells by Cs Substitution. *J. Mater. Chem. A* **2016**, *4* (46), 17939–17945.
(29) Tsai, K.-W.; Chueh, C.-C.; Williams, S. T.; Wen, T.-C.; Jen, A. K. Y. High-Performance Hole-Transporting Layer-Free Conventional Perovskite/Fullerene Heterojunction Thin-Film Solar Cells. *J. Mater. Chem. A* **2015**, *3* (17), 9128–9132.
(30) Xu, B.; Zhu, Z.; Zhang, J.; Liu, H.; Chueh, C.-C.; Li, X.; Jen, A. K.-Y. 4- Tert - Butylpyridine Free Organic Hole Transporting Materials for Stable and Efficient Planar Perovskite Solar Cells. *Adv. Energy Mater.* **2017**, *7* (19), 1700683.
(31) Zhu, Z.; Xu, J.-Q.; Chueh, C.-C.; Liu, H.; Li, Z.; Li, X.; Chen, H.; Jen, A. K.-Y. A Low-Temperature, Solution-Processable Organic Electron-Transporting Layer Based on Planar Coronene for High-Performance Conventional Perovskite Solar Cells. *Adv. Mater.* **2016**, *28* (48), 10786–10793.
(32) Wang, Q.; Lin, F.; Chueh, C.-C.; Zhao, T.; Eslamian, M.; Jen, A. K.-Y. Enhancing Efficiency of Perovskite Solar Cells by Reducing Defects through Imidazolium Cation Incorporation. *Mater. Today Energy* **2017**, 3–10.
(33) Zhao, T.; Chueh, C.-C.; Chen, Q.; Rajagopal, A.; Jen, A. K.-Y. Defect Passivation of Organic–Inorganic Hybrid Perovskites by Diammonium Iodide toward High-Performance Photovoltaic Devices. *ACS Energy Lett.* **2016**, *1* (4), 757–763.
(34) Huang, J.; Carpenter, J. H.; Li, C.-Z.; Yu, J.-S.; Ade, H.; Jen, A. K.-Y. Highly Efficient Organic Solar Cells with Improved Vertical Donor-Acceptor Compositional Gradient Via an Inverted Off-Center Spinning Method. *Adv. Mater.* **2016**, *28* (5), 967–974.
(35) Williams, S. T.; Rajagopal, A.; Jo, S. B.; Chueh, C.-C.; Tang, T. F. L.; Kraeger, A.; Jen, A. K.-Y. Realizing a New Class of Hybrid Organic–inorganic Multifunctional Perovskite. *J. Mater. Chem. A* **2017**, *5* (21), 10640–10650.
(36) Li, Z.; Zhu, Z.; Chueh, C.-C.; Jo, S. B.; Luo, J.; Jang, S.-H.; Jen, A. K.-Y. Rational Design of Dipolar Chromophore as an Efficient Dopant-Free Hole-Transporting Material for Perovskite Solar Cells. *J. Am. Chem. Soc.* **2016**, *138* (36), 11833–11839.
(37) Liu, X.; Tsai, K.; Zhu, Z.; Sun, Y.; Chueh, C.; Jen, A. K. -Y. A Low-Temperature, Solution Processable Tin Oxide Electron-Transporting Layer Prepared by the Dual-Fuel Combustion Method for Efficient Perovskite Solar Cells. *Adv. Mater. Interfaces* **2016**, *3* (13), 1600122.
(38) Jung, J. W.; Chueh, C.; Jen, A. K.-Y. A Low-Temperature, Solution-Processable, Cu-Doped Nickel Oxide Hole-Transporting Layer via the Combustion Method for High-Performance Thin-Film Perovskite Solar Cells. *Adv. Mater.* **2015**, *27* (47), 7874–7880.
(39) Yu, J.; Xi, Y.; Chueh, C.-C.; Xu, J.-Q.; Zhong, H.; Lin, F.; Jo, S. B.; Pozzo, L. D.; Tang, W.; Jen, A. K.-Y. Boosting Performance of Inverted Organic Solar Cells by Using a Planar Coronene Based Electron-Transporting Layer. *Nano Energy* **2017**, *39* (May), 454–460.
(40) Li, N.; Zhu, Z.; Chueh, C.; Liu, H.; Peng, B.; Petrone, A.; Li, X.; Wang, L.; Jen, A. K.-Y. Mixed Cation FA x PEA 1- x PbI 3 with Enhanced Phase and Ambient Stability toward High-Performance Perovskite Solar Cells. *Adv. Energy Mater.* **2017**, *7* (1), 1601307.
(41) Liu, X.; Lin, F.; Chueh, C.-C.; Chen, Q.; Zhao, T.; Liang, P.-W.; Zhu, Z.; Sun, Y.; Jen, A. K.-Y. Fluoroalkyl-Substituted Fullerene/Perovskite Heterojunction for Efficient and Ambient Stable Perovskite Solar Cells. *Nano Energy* **2016**, *30* (October), 417–425.

(42) Chueh, C.; Li, C.; Jen, A. K.-Y. Recent Progress and Perspective in Solution-Processed Interfacial Materials for Efficient and Stable Polymer and Organometal Perovskite Solar Cells. *Energy Environ. Sci.* **2015**, *8* (4), 1160–1189.
(43) Wang, Y.; Zhu, Z.; Chueh, C.-C.; Jen, A. K.-Y.; Chi, Y. Spiro-Phenylpyrazole-9,9′-Thioxanthene Analogues as Hole-Transporting Materials for Efficient Planar Perovskite Solar Cells. *Adv. Energy Mater.* **2017**, *7* (19), 1700823.
(44) Wang, Q.; Chueh, C.-C.; Zhao, T.; Cheng, J.; Eslamian, M.; Choy, W. C. H.; Jen, A. K.-Y. Effects of Self-Assembled Monolayer Modification of Nickel Oxide Nanoparticles Layer on the Performance and Application of Inverted Perovskite Solar Cells. *ChemSusChem* **2017**, *10* (19), 3794–3803.
(45) Zhu, Z.; Chueh, C.-C.; Lin, F.; Jen, A. K.-Y. Enhanced Ambient Stability of Efficient Perovskite Solar Cells by Employing a Modified Fullerene Cathode Interlayer. *Adv. Sci.* **2016**, *3* (9), 1600027.
(46) Zhao, D.; Zhu, Z.; Kuo, M.-Y.; Chueh, C.-C.; Jen, A. K.-Y. Hexaazatrinaphthylene Derivatives: Efficient Electron-Transporting Materials with Tunable Energy Levels for Inverted Perovskite Solar Cells. *Angew. Chemie Int. Ed.* **2016**, *55* (31), 8999–9003.
(47) Li, N.; Zhu, Z.; Dong, Q.; Li, J.; Yang, Z.; Chueh, C.; Jen, A. K.-Y.; Wang, L. Enhanced Moisture Stability of Cesium-Containing Compositional Perovskites by a Feasible Interfacial Engineering. *Adv. Mater. Interfaces* **2017**, *4* (20), 1700598.
(48) Yen, H.-J.; Liang, P.-W.; Chueh, C.-C.; Yang, Z.; Jen, A. K.-Y.; Wang, H.-L. Large Grained Perovskite Solar Cells Derived from Single-Crystal Perovskite Powders with Enhanced Ambient Stability. *ACS Appl. Mater. Interfaces* **2016**, *8* (23), 14513–14520.
(49) Yang, Z.; Rajagopal, A.; Jen, A. K.-Y. Ideal Bandgap Organic-Inorganic Hybrid Perovskite Solar Cells. *Adv. Mater.* **2017**, *29* (47), 1704418.
(50) Liang, P.-W.; Chueh, C.-C.; Williams, S. T.; Jen, A. K.-Y. Roles of Fullerene-Based Interlayers in Enhancing the Performance of Organometal Perovskite Thin-Film Solar Cells. *Adv. Energy Mater.* **2015**, *5* (10), 1402321.
(51) Uhl, A. R.; Yang, Z.; Jen, A. K.-Y.; Hillhouse, H. W. Solution-Processed Chalcopyrite–perovskite Tandem Solar Cells in Bandgap-Matched Two- and Four-Terminal Architectures. *J. Mater. Chem. A* **2017**, *5* (7), 3214–3220.
(52) Williams, S. T.; Chueh, C.; Jen, A. K.-Y. Navigating Organo-Lead Halide Perovskite Phase Space via Nucleation Kinetics toward a Deeper Understanding of Perovskite Phase Transformations and Structure-Property Relationships. *Small* **2015**, *11* (26), 3088–3096.
(53) Zhu, Z.; Chueh, C.-C.; Zhang, G.; Huang, F.; Yan, H.; Jen, A. K.-Y. Improved Ambient-Stable Perovskite Solar Cells Enabled by a Hybrid Polymeric Electron-Transporting Layer. *ChemSusChem* **2016**, *9* (18), 2586–2591.
(54) Rajagopal, A.; Yang, Z.; Jo, S. B.; Braly, I. L.; Liang, P.-W.; Hillhouse, H. W.; Jen, A. K.-Y. Highly Efficient Perovskite-Perovskite Tandem Solar Cells Reaching 80% of the Theoretical Limit in Photovoltage. *Adv. Mater.* **2017**, *29* (34), 1702140.
(55) Uhl, A. R.; Rajagopal, A.; Clark, J. A.; Murray, A.; Feurer, T.; Buecheler, S.; Jen, A. K.-Y.; Hillhouse, H. W. Solution-Processed Low-Bandgap CuIn(S,Se) 2 Absorbers for High-Efficiency Single-Junction and Monolithic Chalcopyrite-Perovskite Tandem Solar Cells. *Adv. Energy Mater.* **2018**, *8* (27), 1801254.
(56) Zhu, Z.; Chueh, C.; Li, N.; Mao, C.; Jen, A. K.-Y. Realizing Efficient Lead-Free Formamidinium Tin Triiodide Perovskite Solar Cells via a Sequential Deposition Route. *Adv. Mater.* **2018**, *30* (6), 1703800.

(57) Yang, Z.; Rajagopal, A.; Chueh, C.; Jo, S. B.; Liu, B.; Zhao, T.; Jen, A. K.-Y. Stable Low-Bandgap Pb-Sn Binary Perovskites for Tandem Solar Cells. *Adv. Mater.* **2016**, *28* (40), 8990–8997.
(58) Zhao, T.; Liu, H.; Ziffer, M. E.; Rajagopal, A.; Zuo, L.; Ginger, D. S.; Li, X.; Jen, A. K. Y. Realization of a Highly Oriented MAPbBr 3 Perovskite Thin Film via Ion Exchange for Ultrahigh Color Purity Green Light Emission. ACS Energy Lett. 2018, 3 (7), 1662–1669.
(59) Tosun, B. S.; Hillhouse, H. W., Enhanced carrier lifetimes of pure iodide hybrid perovskite via vapor-equilibrated re-growth (VERG). The journal of physical chemistry letters 2015, 6 (13), 2503-2508.
(60) Braly, I. L.; Hillhouse, H. W., Optoelectronic Quality and Stability of Hybrid Perovskites from MAPbI3 to MAPbI2Br Using Composition Spread Libraries. The Journal of Physical Chemistry C 2016, 120 (2), 893-902.
(61) Stoddard, R. J.; Eickemeyer, F. T.; Katahara, J. K.; Hillhouse, H. W., Correlation Between Photoluminescence and Carrier Transport and a Simple In-Situ Passivation Method for High-Bandgap Hybrid Perovskites. The Journal of Physical Chemistry Letters 2017.
(62) Braly, I. L.; deQuilettes, D. W.; Pazos-Outon, L. M.; Burke, S.; Ziffer, M. E.; Ginger, D. S.; Hillhouse, H. W., Hybrid Perovskite Films Approaching the Radiative Limit with over 90% Internal Photoluminescence Quantum Efficiency. Nature Photonics 2018.
(63) Williamson, W.; Eickemeyer, F.; Hillhouse, H., Solution Processed BiI3 Films with 1.1 eV Quasi-Fermi Level Splitting: Role of Water, Temperature, and Solvent During Processing. ACS Omega 2018.

Acknowledgment: This material is based upon work supported by the Department of Energy under award number DE-EE0006710

References:

1. Green, M.; Emery, K.; Hishikawa, Y.; Warta, W.; Dunlop, E. D., Solar cell efficiency talbes (version 48). *Progress in Photovoltaics: Research and Applications* **2016,** *24*, 905-913.
2. Green, M. A.; Ho-Baillie, A.; Snaith, H. J., The emergence of perovskite solar cells. *Nature Photonics* **2014,** *8* (7), 506-514.
3. Saliba, M.; Matsui, T.; Domanski, K.; Seo, J.-Y.; Ummadisingu, A.; Zakeeruddin, S. M.; Correa-Baena, J.-P.; Tress, W. R.; Abate, A.; Hagfeldt, A.; Grätzel, M., Incorporation of rubidium cations into perovskite solar cells improves photovoltaic performance. *Science* **2016**.
4. Powell, D. M.; Fu, R.; Horowitz, K.; Basore, P. A.; Woodhouse, M.; Buonassisi, T., The capital intensity of photovoltaics manufacturing: barrier to scale and opportunity for innovation. *Energy & Environmental Science* **2015,** *8* (12), 3395-3408.
5. Yin, W. J.; Shi, T.; Yan, Y., Unique properties of halide perovskites as possible origins of the superior solar cell performance. *Adv Mater* **2014,** *26* (27), 4653-8.
6. Yin, W.-J.; Shi, T.; Yan, Y., Unusual defect physics in CH3NH3PbI3 perovskite solar cell absorber. *Applied Physics Letters* **2014,** *104* (6), 063903.
7. Yu, Y.; Wang, C.; Grice, C. R.; Shrestha, N.; Zhao, D.; Liao, W.; Guan, L.; Awni, R. A.; Meng, W.; Cimaroli, A. J.; Zhu, K.; Ellingson, R. J.; Yan, Y., Synergistic Effects of Lead Thiocyanate Additive and Solvent Annealing on the Performance of Wide-Bandgap Perovskite Solar Cells. *ACS Energy Letters* **2017,** *2*, 1177-1182.
8. Brandt, R. E.; Stevanović, V.; Ginley, D. S.; Buonassisi, T., Identifying defect-tolerant semiconductors with high minority-carrier lifetimes: beyond hybrid lead halide perovskites. *MRS Communications* **2015,** *5* (02), 265-275.
9. Brandt, R. E.; Poindexter, J. R.; Gorai, P.; Kurchin, R. C.; Hoye, R. L.; Nienhaus, L.; Wilson, M. W.; Polizzotti, J. A.; Sereika, R.; Žaltauskas, R., Searching for "defect-tolerant" photovoltaic materials: Combined theoretical and experimental screening. *Chemistry of Materials* **2017**.
10. Forgács, D.; Gil-Escrig, L.; Pérez-Del-Rey, D.; Momblona, C.; Werner, J.; Niesen, B.; Ballif, C.; Sessolo, M.; Bolink, H. J., Efficient monolithic perovskite/perovskite tandem solar cells. *Advanced Energy Materials* **2017,** *7* (8).
11. McMeekin, D. P.; Sadoughi, G.; Rehman, W.; Eperon, G. E.; Saliba, M.; Hörantner, M. T.; Haghighirad, A.; Sakai, N.; Korte, L.; Rech, B.; Johnston, M. B.; Herz, L. M.; Snaith, H. J., A mixed-cation lead mixed-halide perovskite absorber for tandem solar cells. *Science* **2016,** *351* (6269), 151-155.
12. Noh, J. H.; Im, S. H.; Heo, J. H.; Mandal, T. N.; Seok, S. I., Chemical management for colorful, efficient, and stable inorganic-organic hybrid nanostructured solar cells. *Nano Lett* **2013,** *13* (4), 1764-9.
13. Eperon, G. E.; Leijtens, T.; Bush, K. A.; Prasanna, R.; Green, T.; Wang, J. T.-W.; McMeekin, D. P.; Volonakis, G.; Milot, R. L.; May, R.; Palmstrom, A.; Slotcavage, D. J.; Belisle, R. A.; Patel, J. B.; Parrott, E. S.; Sutton, R. J.; Ma, W.; Moghadam, F.; Conings, B.; Babayigit, A.; Boyen, H.-G.; Bent, S.; Giustino, F.; Herz, L. M.; Johnston, M. B.; McGehee, M. D.; Snaith, H. J., Perovskite-perovskite tandem photovoltaics with optimized band gaps. *Science* **2016,** *354* (6314), 861-865.
14. Rajagopal, A.; Yang, Z.; Jo, S. B.; Braly, I. L.; Liang, P. W.; Hillhouse, H. W.; Jen, A. K. Y., Highly Efficient Perovskite–Perovskite Tandem Solar Cells Reaching 80% of the Theoretical Limit in Photovoltage. *Advanced Materials* **2017,** *29* (34).

15. Yang, Z.; Rajagopal, A.; Chueh, C. C.; Jo, S. B.; Liu, B.; Zhao, T.; Jen, A. K. Y., Stable Low-Bandgap Pb–Sn Binary Perovskites for Tandem Solar Cells. *Advanced Materials* **2016,** *28* (40), 8990-8997.
16. Jesper Jacobsson, T.; Correa-Baena, J.-P.; Pazoki, M.; Saliba, M.; Schenk, K.; Grätzel, M.; Hagfeldt, A., Exploration of the compositional space for mixed lead halogen perovskites for high efficiency solar cells. *Energy Environ. Sci.* **2016**.
17. Bush, K. A.; Palmstrom, A. F.; Yu, Z. J.; Boccard, M.; Cheacharoen, R.; Mailoa, J. P.; McMeekin, D. P.; Hoye, R. L. Z.; Bailie, C. D.; Leijtens, T.; Peters, I. M.; Minichetti, M. C.; Rolston, N.; Prasanna, R.; Sofia, S.; Harwood, D.; Ma, W.; Moghadam, F.; Snaith, H. J.; Buonassisi, T.; Holman, Z. C.; Bent, S. F.; McGehee, M. D., 23.6%-efficient monolithic perovskite/silicon tandem solar cells with improved stability. *Nature Energy* **2017,** *2*.
18. Uhl, A. R.; Yang, Z.; Jen, A. K.-Y.; Hillhouse, H. W., Solution-processed chalcopyrite–perovskite tandem solar cells in bandgap-matched two- and four-terminal architectures. *Journal of Materials Chemistry A* **2017,** (7).
19. Hörantner, M. T.; Leijtens, T.; Ziffer, M. E.; Eperon, G. E.; Christoforo, M. G.; McGehee, M. D.; Snaith, H. J., The Potential of Multi-Junction Perovskite Solar Cells. *ACS Energy Letters* **2017**.
20. Bailie, C. D.; McGehee, M. D., High-efficiency tandem perovskite solar cells. *Mrs Bulletin* **2015,** *40* (8), 681-686.
21. Stoddard, R. J.; Rajagopal, A.; Palmer, R. L.; Braly, I. L.; Jen, A. K. Y.; Hillhouse, H. W., Enhancing Defect Tolerance and Phase Stability of High-Bandgap Perovskites via Guanidinium Alloying. *ACS Energy Letters* **2018**.
22. Rehman, W.; McMeekin, D. P.; Patel, J. B.; Milot, R. L.; Johnston, M. B.; Snaith, H. J.; Herz, L. M., Photovoltaic mixed-cation lead mixed-halide perovskites: links between crystallinity, photo-stability and electronic properties. *Energy and Environmental Science* **2017,** *10*, 361-369.
23. Stoddard, R. J.; Eickemeyer, F. T.; Katahara, J. K.; Hillhouse, H. W., Correlation between Photoluminescence and Carrier Transport and a Simple In Situ Passivation Method for High-Bandgap Hybrid Perovskites. *The Journal of Physical Chemistry Letters* **2017,** *8* (14), 3289-3298.
24. Hoke, E. T.; Slotcavage, D. J.; Dohner, E. R.; Bowring, A. R.; Karunadasa, H. I.; McGehee, M. D., Reversible photo-induced trap formation in mixed-halide hybrid perovskites for photovoltaics. *Chemical Science* **2015,** *6* (1), 613-617.
25. Braly, I. L.; Stoddard, R. J.; Rajagopal, A.; Uhl, A. R.; Katahara, J. K.; Jen, A. K.-Y.; Hillhouse, H. W., Current-Induced Phase Segregation in Mixed Halide Hybrid Perovskites and its Impact on Two-Terminal Tandem Solar Cell Design. **2017**.
26. Yang, Z.; Rajagopal, A.; Jo, S. B.; Chueh, C.-C.; Williams, S.; Huang, C.-C.; Katahara, J. K.; Hillhouse, H. W.; Jen, A. K.-Y., Stabilized Wide Bandgap Perovskite Solar Cells by Tin Substitution. *Nano Letters* **2016,** *16* (12), 7739-7747.
27. Yang, M.; Kim, D. H.; Yu, Y.; Li, Z.; Reid, O. G.; Song, Z.; Zhao, D.; Wang, C.; Li, L.; Meng, Y., Effect of non-stoichiometric solution chemistry on improving the performance of wide-bandgap perovskite solar cells. *Materials Today Energy* **2017**.
28. Zhou, Y.; Wang, F.; Cao, Y.; Wang, J. P.; Fang, H. H.; Loi, M. A.; Zhao, N.; Wong, C. P., Benzylamine-Treated Wide-Bandgap Perovskite with High Thermal-Photostability and Photovoltaic Performance. *Advanced Energy Materials* **2017,** *7* (22).

29. Braly, I. L.; Hillhouse, H. W., Optoelectronic Quality and Stability of Hybrid Perovskites from MAPbI3to MAPbI2Br Using Composition Spread Libraries. *The Journal of Physical Chemistry C* **2016,** *120* (2), 893-902.
30. Duong, T.; Wu, Y.; Shen, H.; Peng, J.; Fu, X.; Jacobs, D.; Wang, E.-C.; Kho, T. C.; Fong, K. C.; Stocks, M.; Franklin, E.; Blakers, A.; Zin, N.; McIntosh, K.; Li, W.; Cheng, Y.-B.; White, T. P.; Weber, K.; Catchpole, K., Rubidium Multication Perovskite with Optimized Bandgap for Perovskite-Silicon Tandem with over 26% Efficiency. *Advanced Energy Materials* **2017**.
31. Slotcavage, D. J.; Karunadasa, H. I.; McGehee, M. D., Light-Induced Phase Segregation in Halide-Perovskite Absorbers. *ACS Energy Letters* **2016,** *1* (6), 1199–1205.
32. Brennan, M. C.; Draguta, S.; Kamat, P. V.; Kuno, M., Light-Induced Anion Phase Segregation in Mixed Halide Perovskites. *ACS Energy Letters* **2017**.
33. Tang, X.; Brandl, M.; May, B.; Levchuk, I.; Hou, Y.; Richter, M.; Chen, H.; Chen, S.; Kahmann, S.; Osvet, A.; Maier, F.; Steinrück, H.-P.; Hock, R.; Matt, G. J.; Brabec, C. J., Photoinduced degradation of methylammonium lead triiodide perovskite semiconductors. *Journal of Materials Chemistry A* **2016,** *4*, 15896-15903.
34. Huang, W.; Manser, J. S.; Kamat, P. V.; Ptasinska, S., Evolution of Chemical Composition, Morphology, and Photovoltaic Efficiency of CH3NH3PbI3 Perovskite under Ambient Conditions. *Chemistry of Materials* **2016,** *28* (1), 303-311.
35. Aristidou, N.; Sanchez-Molina, I.; Chotchuangchutchaval, T.; Brown, M.; Martinez, L.; Rath, T.; Haque, S. A., The role of oxygen in the degradation of methylammonium lead trihalide perovskite photoactive layers. *Angewandte Chemie International Edition* **2015,** *54* (28), 8208-8212.
36. Aristidou, N.; Eames, C.; Sanchez-Molina, I.; Bu, X.; Kosco, J.; Islam, M. S.; Haque, S. A., Fast oxygen diffusion and iodide defects mediate oxygen-induced degradation of perovskite solar cells. *Nature Communications* **2017,** *8*.
37. Chen, S.; Hou, Y.; Chen, H.; Tang, X.; Langner, S.; Li, N.; Stubhan, T.; Levchuk, I.; Gu, E.; Osvet, A., Exploring the Stability of Novel Wide Bandgap Perovskites by a Robot Based High Throughput Approach. *Advanced Energy Materials* **2017**.
38. Bush, K. A.; Bailie, C. D.; Chen, Y.; Bowring, A. R.; Wang, W.; Ma, W.; Leijtens, T.; Moghadam, F.; McGehee, M. D., Thermal and Environmental Stability of Semi-Transparent Perovskite Solar Cells for Tandems Enabled by a Solution-Processed Nanoparticle Buffer Layer and Sputtered ITO Electrode. *Advanced Materials* **2016,** *28* (20), 3937-3943.
39. Leijtens, T.; Bush, K.; Cheacharoen, R.; Beal, R.; Bowring, A.; McGehee, M. D., Towards enabling stable lead halide perovskite solar cells; interplay between structural, environmental, and thermal stability. *Journal of Materials Chemistry A* **2017**.
40. Abdi-Jalebi, M.; Andaji-Garmaroudi, Z.; Cacovich, S.; Stavrakas, C.; Philippe, B.; Richter, J. M.; Alsari, M.; Booker, E. P.; Hutter, E. M.; Pearson, A. J., Maximising and Stabilising Luminescence in Metal Halide Perovskite Device Structures. *arXiv preprint arXiv:1712.04696* **2017**.
41. DOE, Solar Energy Technologies Office (SETO) FY2018
Funding Opportunity Announcement (FOA) 2018.
42. Bush, K. A.; Palmstrom, A. F.; Yu, Z. J.; Boccard, M.; Cheacharoen, R.; Mailoa, J. P.; McMeekin, D. P.; Hoye, R. L. Z.; Bailie, C. D.; Leijtens, T.; Peters, I. M.; Minichetti, M. C.; Rolston, N.; Prasanna, R.; Sofia, S.; Harwood, D.; Ma, W.; Moghadam, F.; Snaith, H. J.;

Buonassisi, T.; Holman, Z. C.; Bent, S. F.; McGehee, M. D., 23.6%-efficient monolithic perovskite/silicon tandem solar cells with improved stability. *Nature Energy* **2017,** *2*, 17009.
43. Albrecht, S.; Saliba, M.; Baena, J. P. C.; Lang, F.; Kegelmann, L.; Mews, M.; Steier, L.; Abate, A.; Rappich, J.; Korte, L.; Schlatmann, R.; Nazeeruddin, M. K.; Hagfeldt, A.; Gratzel, M.; Rech, B., Monolithic perovskite/silicon-heterojunction tandem solar cells processed at low temperature. *Energy & Environmental Science* **2016,** *9* (1), 81-88.
44. Werner, J.; Barraud, L.; Walter, A.; Bräuninger, M.; Sahli, F.; Sacchetto, D.; Tétreault, N.; Paviet-Salomon, B.; Moon, S.-J.; Allebé, C.; Despeisse, M.; Nicolay, S.; Wolf, S. D.; Niesen, B.; Ballif, C., Efficient Near-Infrared-Transparent Perovskite Solar Cells Enabling Direct Comparison of 4-Terminal and Monolithic Perovskite/Silicon Tandem Cells. *ACS Energy Letters* **2016,** *1* (2), 474–480.
45. Werner, J.; Weng, C. H.; Walter, A.; Fesquet, L.; Seif, J. P.; De Wolf, S.; Niesen, B.; Ballif, C., Efficient Monolithic Perovskite/Silicon Tandem Solar Cell with Cell Area > 1 cm(2). *Journal of Physical Chemistry Letters* **2016,** *7* (1), 161-166.
46. Su, Z. H.; Sun, K. W.; Han, Z. L.; Cui, H. T.; Liu, F. Y.; Lai, Y. Q.; Li, J.; Hao, X. J.; Liu, Y. X.; Green, M. A., Fabrication of Cu2ZnSnS4 solar cells with 5.1% efficiency via thermal decomposition and reaction using a non-toxic sol-gel route. *Journal of Materials Chemistry A* **2014,** *2* (2), 500-509.
47. Todorov, T.; Gershon, T.; Gunawan, O.; Lee, Y. S.; Sturdevant, C.; Chang, L.-Y.; Guha, S., Monolithic Perovskite-CIGS Tandem Solar Cells via In Situ Band Gap Engineering. *Advanced Energy Materials* **2015**, n/a-n/a.
48. Eperon, G. E.; Leijtens, T.; Bush, K. A.; Prasanna, R.; Green, T.; Wang, J. T. W.; McMeekin, D. P.; Volonakis, G.; Milot, R. L.; May, R.; Palmstrom, A.; Slotcavage, D. J.; Belisle, R. A.; Patel, J. B.; Parrott, E. S.; Sutton, R. J.; Ma, W.; Moghadam, F.; Conings, B.; Babayigit, A.; Boyen, H. G.; Bent, S.; Giustino, F.; Herz, L. M.; Johnston, M. B.; McGehee, M. D.; Snaith, H. J., Perovskite-perovskite tandem photovoltaics with optimized band gaps. *Science* **2016,** *354* (6314), 861-865.
49. Rajagopal, A.; Yang, Z.; Jo, S. B.; Braly, I. L.; Liang, P.-W.; Hillhouse, H. W.; Jen, A. K.-Y., 80% of Theoretical Limit in Photovoltage realized for Perovskite-Perovskite Tandem Solar Cells. *Advanced Materials* **2017**.
50. Kayes, B. M.; Zhang, L.; Twist, R.; Ding, I. K.; Higashi, G. S., Flexible Thin-Film Tandem Solar Cells With >30% Efficiency. *IEEE Journal of Photovoltaics* **2014,** *4* (2), 729-733.
51. Chen, B.; Zheng, X.; Bai, Y.; Padture, N. P.; Huang, J., Progress in Tandem Solar Cells Based on Hybrid Organic–Inorganic Perovskites. *Advanced Energy Materials* **2017**, 1602400-n/a.
52. Saliba, M.; Matsui, T.; Domanski, K.; Seo, J. Y.; Ummadisingu, A.; Zakeeruddin, S. M.; Correa-Baena, J. P.; Tress, W. R.; Abate, A.; Hagfeldt, A.; Gratzel, M., Incorporation of rubidium cations into perovskite solar cells improves photovoltaic performance. *Science* **2016,** *354* (6309), 206-209.
53. McMeekin, D. P.; Sadoughi, G.; Rehman, W.; Eperon, G. E.; Saliba, M.; Horantner, M. T.; Haghighirad, A.; Sakai, N.; Korte, L.; Rech, B.; Johnston, M. B.; Herz, L. M.; Snaith, H. J., A mixed-cation lead mixed-halide perovskite absorber for tandem solar cells. *Science* **2016,** *351* (6269), 151-155.
54. Yu, Y.; Wang, C.; Grice, C. R.; Shrestha, N.; Zhao, D.; Liao, W.; Guan, L.; Awni, R. A.; Meng, W.; Cimaroli, A. J.; Zhu, K.; Ellingson, R. J.; Yan, Y., Synergistic Effects of Lead Thiocyanate Additive and Solvent Annealing on the Performance of Wide-Bandgap Perovskite Solar Cells. *ACS Energy Letters* **2017,** *2* (5), 1177-1182.

55. Noh, J. H.; Im, S. H.; Heo, J. H.; Mandal, T. N.; Seok, S. I., Chemical management for colorful, efficient, and stable inorganic-organic hybrid nanostructured solar cells. *Nano Letters* **2013,** *13* (4), 1764-1769.
56. Suarez, B.; Gonzalez-Pedro, V.; Ripolles, T. S.; Sanchez, R. S.; Otero, L.; Mora-Sero, I., Recombination Study of Combined Halides (Cl, Br, I) Perovskite Solar Cells. *The Journal of Physical Chemistry Letters* **2014,** *5* (10), 1628-1635.
57. Unger, E. L.; Kegelmann, L.; Suchan, K.; Sorell, D.; Korte, L.; Albrecht, S., Roadmap and roadblocks for the band gap tunability of metal halide perovskites. *Journal of Materials Chemistry A* **2017**.
58. Yang, Z. B.; Rajagopal, A.; Jo, S. B.; Chueh, C. C.; Williams, S.; Huang, C. C.; Katahara, J. K.; Hillhouse, H. W.; Jen, A. K. Y., Stabilized Wide Bandgap Perovskite Solar Cells by Tin Substitution. *Nano Letters* **2016,** *16* (12), 7739-7747.
59. Slotcavage, D. J.; Karunadasa, H. I.; McGehee, M. D., Light-Induced Phase Segregation in Halide-Perovskite Absorbers. *ACS Energy Letters* **2016,** *1* (6), 1199-1205.
60. Hu, M.; Bi, C.; Yuan, Y.; Bai, Y.; Huang, a. J., Stabilized Wide Bandgap MAPbBrxI3–x Perovskite by Enhanced Grain Size and Improved Crystallinity. *Advanced Science* **2016,** *3* (1500301).
61. Duong, T.; Wu, Y.; Shen, H.; Peng, J.; Fu, X.; Jacobs, D.; Wang, E.-C.; Kho, T. C.; Fong, K. C.; Stocks, M.; Franklin, E.; Blakers, A.; Zin, N.; McIntosh, K.; Li, W.; Cheng, Y.-B.; White, T. P.; Weber, K.; Catchpole, K., Rubidium Multication Perovskite with Optimized Bandgap for Perovskite-Silicon Tandem with over 26% Efficiency. *Advanced Energy Materials* **2017**, 1700228-n/a.
62. Beal, R. E.; Slotcavage, D. J.; Leijtens, T.; Bowring, A. R.; Belisle, R. A.; Nguyen, W. H.; Burkhard, G. F.; Hoke, E. T.; McGehee, M. D., Cesium Lead Halide Perovskites with Improved Stability for Tandem Solar Cells. *J Phys Chem Lett* **2016,** *7* (5), 746-51.
63. Forgacs, D.; Perez-del-Rey, D.; Avila, J.; Momblona, C.; Gil-Escrig, L.; Danekamp, B.; Sessolo, M.; Bolink, a. H. J., Efficient wide band gap double cation – double halide perovskite solar cells. *Journal of Materials Chemistry A* **2017,** *5*, 3203-3207.
64. Ndione, P. F.; Li, Z.; Zhu, K., Effects of alloying on the optical properties of organic–inorganic lead halide perovskite thin films. *Journal of Materials Chemistry C* **2016,** *4*, 7775-7782.
65. Bischak, C. G.; Hetherington, C. L.; Wu, H.; Aloni, S.; Ogletree, D. F.; Limmer, D. T.; Ginsberg, N. S., Origin of Reversible Photoinduced Phase Separation in Hybrid Perovskites. *Nano Letters* **2017,** *17* (2), 1028-1033.
66. Aristidou, N.; Sanchez-Molina, I.; Chotchuangchutchaval, T.; Brown, M.; Martinez, L.; Rath, T.; Haque, S. A., The Role of Oxygen in the Degradation of Methylammonium Lead Trihalide Perovskite Photoactive Layers. *Angewandte Chemie-International Edition* **2015,** *54* (28), 8208-8212.
67. Bryant, D.; Aristidou, N.; Pont, S.; Sanchez-Molina, I.; Chotchunangatchaval, T.; Wheeler, S.; Durrant, J. R.; Haque, S. A., Light and oxygen induced degradation limits the operational stability of methylammonium lead triiodide perovskite solar cells. *Energy & Environmental Science* **2016,** *9* (5), 1655-1660.
68. Tan, H.; Che, F.; Wei, M.; Zhao, Y.; Saidaminov, M. I.; Todorović, P.; Broberg, D.; Walters, G.; Tan, F.; Zhuang, T., Dipolar cations confer defect tolerance in wide-bandgap metal halide perovskites. *Nature communications* **2018,** *9* (1), 3100.
69. Leijtens, T.; Prasanna, R.; Bush, K. A.; Eperon, G. E.; Raiford, J. A.; Gold-Parker, A.; Wolf, E. J.; Swifter, S. A.; Boyd, C. C.; Wang, H.-P., Tin–lead halide perovskites with improved

thermal and air stability for efficient all-perovskite tandem solar cells. *Sustainable Energy & Fuels* **2018**.
70. Zhou, Y.; Jia, Y. H.; Fang, H. H.; Loi, M. A.; Xie, F. Y.; Gong, L.; Qin, M. C.; Lu, X. H.; Wong, C. P.; Zhao, N., Composition-Tuned Wide Bandgap Perovskites: From Grain Engineering to Stability and Performance Improvement. *Advanced Functional Materials* **2018,** *28* (35), 1803130.
71. Luo, D.; Yang, W.; Wang, Z.; Sadhanala, A.; Hu, Q.; Su, R.; Shivanna, R.; Trindade, G. F.; Watts, J. F.; Xu, Z., Enhanced photovoltage for inverted planar heterojunction perovskite solar cells. *Science* **2018,** *360* (6396), 1442-1446.
72. Stolterfoht, M.; Wolff, C. M.; Márquez, J. A.; Zhang, S.; Hages, C. J.; Rothhardt, D.; Albrecht, S.; Burn, P. L.; Meredith, P.; Unold, T., Visualization and suppression of interfacial recombination for high-efficiency large-area pin perovskite solar cells. *Nature Energy* **2018,** *3* (10), 847.
73. Braly, I. L.; Hillhouse, H. W., Optoelectronic Quality and Stability of Hybrid Perovskites from MAPbI3 to MAPbI2Br Using Composition Spread Libraries. *The Journal of Physical Chemistry C* **2016,** *120* (2), 893-902.
74. Stoddard, R. J.; Rajagopal, A.; Palmer, R. L.; Braly, I. L.; Jen, A. K.-Y.; Hillhouse, H. W., Enhancing Defect Tolerance and Phase Stability of High-Bandgap Perovskites via Guanidinium Alloying. *ACS Energy Letters* **2018**.
75. Stranks, S. D.; Burlakov, V. M.; Leijtens, T.; Ball, J. M.; Goriely, A.; Snaith, H. J., Recombination Kinetics in Organic-Inorganic Perovskites: Excitons, Free Charge, and Subgap States. *Physical Review Applied* **2014,** *2* (3), 034007.
76. deQuilettes, D. W.; Koch, S.; Burke, S.; Paranji, R. K.; Shropshire, A. J.; Ziffer, M. E.; Ginger, D. S., Photoluminescence Lifetimes Exceeding 8 mu s and Quantum Yields Exceeding 30% in Hybrid Perovskite Thin Films by Ligand Passivation. *Acs Energy Letters* **2016,** *1* (2), 438-444.
77. Noel, N. K.; Abate, A.; Stranks, S. D.; Parrott, E. S.; Burlakov, V. M.; Goriely, A.; Snaith, H. J., Enhanced Photoluminescence and Solar Cell Performance via Lewis Base Passivation of Organic–Inorganic Lead Halide Perovskites. *ACS Nano* **2014**.
78. Fang, H. H.; Wang, F.; Adjokatse, S.; Zhao, N.; Loi, M. A., Photoluminescence enhancement in formamidinium lead iodide thin films. *Advanced Functional Materials* **2016,** *26* (26), 4653-4659.
79. Tian, Y.; Peter, M.; Unger, E.; Abdellah, M.; Zheng, K.; Pullerits, T.; Yartsev, A.; Sundström, V.; Scheblykin, I. G., Mechanistic insights into perovskite photoluminescence enhancement: light curing with oxygen can boost yield thousandfold. *Physical Chemistry Chemical Physics* **2015,** *17* (38), 24978-24987.
80. Zong, Y.; Wang, N.; Zhang, L.; Ju, M.-G.; Zeng, X. C.; Sun, X. W.; Zhou, Y.; Padture, N. P., Homogenous Alloys of Formamidinium Lead Triiodide and Cesium Tin Triiodide for Efficient Ideal-Bandgap Perovskite Solar Cells. *Angewandte Chemie (International ed. in English)* **2017,** *56* (41), 12658-12662.
81. Yang, Z.; Rajagopal, A.; Jen, A. K. Y., Ideal Bandgap Organic–Inorganic Hybrid Perovskite Solar Cells. *Advanced Materials* **2017,** *29* (47).
82. Xi, J.; Wu, Z.; Jiao, B.; Dong, H.; Ran, C.; Piao, C.; Lei, T.; Song, T. B.; Ke, W.; Yokoyama, T., Multichannel Interdiffusion Driven FASnI3 Film Formation Using Aqueous Hybrid Salt/Polymer Solutions toward Flexible Lead-Free Perovskite Solar Cells. *Advanced Materials* **2017,** *29* (23), 1606964.

83. Lee, J.-W.; Kim, H.-S.; Park, N.-G., Lewis acid–base adduct approach for high efficiency perovskite solar cells. *Accounts of chemical research* **2016,** *49* (2), 311-319.
84. Zhu, Z.; Chueh, C. C.; Li, N.; Mao, C.; Jen, A. K. Y., Realizing Efficient Lead-Free Formamidinium Tin Triiodide Perovskite Solar Cells via a Sequential Deposition Route. *Advanced Materials* **2018,** *30* (6), 1703800.
85. Wang, K.; Liu, C.; Du, P.; Zheng, J.; Gong, X., Bulk heterojunction perovskite hybrid solar cells with large fill factor. *Energy & Environmental Science* **2015**.
86. Wang, J., Nanoparticle-based electrochemical DNA detection. *Analytica Chimica Acta* **2003,** *500* (1-2), 247-257.
87. Xu, J.; Buin, A.; Ip, A. H.; Li, W.; Voznyy, O.; Comin, R.; Yuan, M.; Jeon, S.; Ning, Z.; McDowell, J. J.; Kanjanaboos, P.; Sun, J.-P.; Lan, X.; Quan, L. N.; Kim, D. H.; Hill, I. G.; Maksymovych, P.; Sargent, E. H., Perovskite–fullerene hybrid materials suppress hysteresis in planar diodes. *Nature Communications, Published online: 8 May 2015; | doi:10.1038/ncomms8081* **2015**.
88. Braly, I. L.; Stoddard, R. J.; Rajagopal, A.; Uhl, A. R.; Katahara, J. K.; Jen, A. K. y.; Hillhouse, H. W., Current Induced Phase Segregation in Mixed Halide Hybrid Perovskites and its Impact on Two-Terminal Tandem Solar Cell Design. *ACS Energy Letters* **2017**.
89. Jung, J. W.; Chueh, C.-C.; Jen, A. K. Y., High-Performance Semitransparent Perovskite Solar Cells with 10% Power Conversion Efficiency and 25% Average Visible Transmittance Based on Transparent CuSCN as the Hole-Transporting Material. *Advanced Energy Materials* **2015**, n/a-n/a.
90. Liang, P.-W.; Liao, C.-Y.; Chueh, C.-C.; Zuo, F.; Williams, S. T.; Xin, X.-K.; Lin, J.; Jen, A. K. Y., Additive Enhanced Crystallization of Solution-Processed Perovskite for Highly Efficient Planar-Heterojunction Solar Cells. *Advanced Materials* **2014,** *26* (22), 3748-3754.
91. Chueh, C.-C.; Liao, C.-Y.; Zuo, F.; Williams, S. T.; Liang, P.-W.; Jen, A. K. Y., The roles of alkyl halide additives in enhancing perovskite solar cell performance. *Journal of Materials Chemistry A* **2015,** *3* (17), 9058-9062.
92. Liang, P.-W.; Chueh, C.-C.; Xin, X.-K.; Zuo, F.; Williams, S. T.; Liao, C.-Y.; Jen, A. K. Y., High-Performance Planar-Heterojunction Solar Cells Based on Ternary Halide Large-Band-Gap Perovskites. *Advanced Energy Materials* **2015,** *5* (1), n/a-n/a.
93. Zuo, F.; Williams, S. T.; Liang, P.-W.; Chueh, C.-C.; Liao, C.-Y.; Jen, A. K. Y., Binary-Metal Perovskites Toward High-Performance Planar-Heterojunction Hybrid Solar Cells. *Advanced Materials* **2014,** *26* (37), 6454-6460.
94. Wang, Q.; Shao, Y.; Dong, Q.; Xiao, Z.; Yuan, Y.; Huang, J., Large fill-factor bilayer iodine perovskite solar cells fabricated by a low-temperature solution-process. *Energy & Environmental Science* **2014,** *7* (7), 2359-2365.
95. You, J.; Hong, Z.; Yang, Y.; Chen, Q.; Cai, M.; Song, T.-B.; Chen, C.-C.; Lu, S.; Liu, Y.; Zhou, H.; Yang, Y., Low-Temperature Solution-Processed Perovskite Solar Cells with High Efficiency and Flexibility. *ACS Nano* **2014,** *8* (2), 1674-1680.
96. Liang, P.-W.; Chueh, C.-C.; Williams, S. T.; Jen, A. K. Y., Roles of Fullerene-Based Interlayers in Enhancing the Performance of Organometal Perovskite Thin-Film Solar Cells. *Advanced Energy Materials* **2015,** *5* (10), n/a-n/a.
97. Braly, I. L.; deQuilettes, D. W.; Pazos-Outon, L. M.; Burke, S.; Ziffer, M. E.; Ginger, D. S.; Hillhouse, H. W., Hybrid Perovskite Films Approaching the Radiative Limit with over 90% Internal Photoluminescence Quantum Efficiency. *Nature Photonics* **2018**.

98. Braly, I. L.; Hillhouse, H. W., Optoelectronic Quality and Stability of Hybrid Perovskites from MAPbI3 to MAPbI2Br Using Composition Spread Libraries. **2016**.
99. Xu, W.; Liao, Y. T.; Akins, D. L., Stabilized Wide Bandgap $MAPbBr_xI3–x$ Perovskite by Enhanced Gra_{in} Size and Improved CrystallinityFormation of CdS nanoparticles within modified MCM-41 and SBA-15. *Journal of Physical Chemistry B* **2002,** *106* (43), 11127-11131.
100. Im, J.; Stoumpos, C. C.; Jin, H.; Freeman, A. J.; Kanatzidis, M. G., Antagonism between Spin–Orbit Coupling and Steric Effects Causes Anomalous Band Gap Evolution in the Perovskite Photovoltaic Materials CH3NH3Sn1–xPbxI3. *The Journal of Physical Chemistry Letters* **2015**.
101. Rajagopal A, Y. Z., Jo SB, Braly IL, Liang PW, Hillhouse HW, Jen AK., Highly Efficient Perovskite–Perovskite Tandem Solar Cells Reaching 80% of the Theoretical Limit in Photovoltage. *Advanced Materials* **2017**.
102. Fu, Y.; Wu, T.; Wang, J.; Zhai, J.; Shearer, M. J.; Zhao, Y.; Hamers, R. J.; Kan, E.; Deng, K.; Zhu, X.-Y., Stabilization of the metastable lead iodide perovskite phase via surface functionalization. *Nano letters* **2017,** *17* (7), 4405-4414.
103. Rajagopal, A.; Stoddard, R. J.; Jo, S. B.; Hillhouse, H. W.; Jen, A. K. Y., Overcoming the Photovoltage Plateau in Large Bandgap Perovskite Photovoltaics. *Nano Letters* **2018**.
104. Uhl, A. R.; Yang, Z. B.; Jen, A. K. Y.; Hillhouse, H. W., Solution-processed chalcopyrite-perovskite tandem solar cells in bandgap-matched two- and four-terminal architectures. *Journal of Materials Chemistry A* **2017,** *5* (7), 3214-3220.